



**HAL**  
open science

## Measuring Cosmological Parameters with Type Ia Supernovae in redMaGiC Galaxies

R. Chen, D. Scolnic, E. Rozo, E.S. Rykoff, B. Popovic, R. Kessler, M. Vincenzi, T.M. Davis, P. Armstrong, D. Brout, et al.

► **To cite this version:**

R. Chen, D. Scolnic, E. Rozo, E.S. Rykoff, B. Popovic, et al.. Measuring Cosmological Parameters with Type Ia Supernovae in redMaGiC Galaxies. *Astrophys.J.*, 2022, 938 (1), pp.62. 10.3847/1538-4357/ac8b82 . hal-03601375

**HAL Id: hal-03601375**

**<https://hal.science/hal-03601375>**

Submitted on 7 Apr 2023

**HAL** is a multi-disciplinary open access archive for the deposit and dissemination of scientific research documents, whether they are published or not. The documents may come from teaching and research institutions in France or abroad, or from public or private research centers.

L'archive ouverte pluridisciplinaire **HAL**, est destinée au dépôt et à la diffusion de documents scientifiques de niveau recherche, publiés ou non, émanant des établissements d'enseignement et de recherche français ou étrangers, des laboratoires publics ou privés.



Distributed under a Creative Commons Attribution 4.0 International License



# Measuring Cosmological Parameters with Type Ia Supernovae in redMaGiC Galaxies

R. Chen<sup>1</sup> , D. Scolnic<sup>1</sup>, E. Rozo<sup>2</sup>, E. S. Rykoff<sup>3,4</sup> , B. Popovic<sup>1</sup> , R. Kessler<sup>5,6</sup> , M. Vincenzi<sup>1</sup>, T. M. Davis<sup>7</sup> ,  
 P. Armstrong<sup>8</sup>, D. Brout<sup>9,10</sup> , L. Galbany<sup>11,12</sup> , L. Kelsey<sup>13,14</sup>, C. Lidman<sup>8,15</sup> , A. Möller<sup>16</sup>, B. Rose<sup>1</sup>, M. Sako<sup>17</sup> ,  
 M. Sullivan<sup>14</sup> , G. Taylor<sup>8</sup>, P. Wiseman<sup>14</sup>, J. Asorey<sup>18</sup>, A. Carr<sup>7</sup> , C. Conselice<sup>19,20</sup> , K. Kuehn<sup>21,22</sup> , G. F. Lewis<sup>23</sup> ,  
 E. Macaulay<sup>13</sup>, M. Rodriguez-Monroy<sup>24</sup>, B. E. Tucker<sup>8</sup> , T. M. C. Abbott<sup>25</sup>, M. Agüena<sup>26</sup> , S. Allam<sup>27</sup>, F. Andrade-Oliveira<sup>28</sup>,  
 J. Annis<sup>27</sup> , D. Bacon<sup>13</sup> , E. Bertin<sup>29,30</sup> , S. Bocquet<sup>31</sup> , D. Brooks<sup>32</sup> , D. L. Burke<sup>3,4</sup>, A. Carnero Rosell<sup>26,33,34</sup>,  
 M. Carrasco Kind<sup>35,36</sup>, J. Carretero<sup>37</sup> , R. Cawthon<sup>38</sup>, M. Costanzi<sup>39,40,41</sup> , L. N. da Costa<sup>26,42</sup>, M. E. S. Pereira<sup>43</sup>, S. Desai<sup>44</sup> ,  
 H. T. Diehl<sup>27</sup> , P. Doel<sup>32</sup>, S. Everett<sup>45</sup>, I. Ferrero<sup>46</sup>, B. Flaugher<sup>27</sup>, D. Friedel<sup>35</sup>, J. Frieman<sup>6,27</sup>, J. García-Bellido<sup>47</sup> , M. Gatti<sup>17</sup>,  
 E. Gaztanaga<sup>11,12</sup> , D. Gruen<sup>31,48</sup> , S. R. Hinton<sup>7</sup> , D. L. Hollowood<sup>45</sup> , K. Honscheid<sup>49,50</sup>, D. J. James<sup>10</sup>, O. Lahav<sup>32</sup>,  
 M. Lima<sup>26,51</sup>, M. March<sup>17</sup>, F. Menanteau<sup>35,36</sup> , R. Miquel<sup>37,52</sup> , R. Morgan<sup>53</sup> , A. Palmese<sup>54</sup> , F. Paz-Chinchón<sup>35,55</sup> ,  
 A. Pieres<sup>26,42</sup> , A. A. Plazas Malagón<sup>56</sup>, J. Prat<sup>5,6</sup>, A. K. Romer<sup>57</sup> , A. Roodman<sup>3,4</sup> , E. Sanchez<sup>18</sup>, M. Schubnell<sup>28</sup>,  
 S. Serrano<sup>11,12</sup> , I. Sevilla-Noarbe<sup>18</sup> , M. Smith<sup>14</sup> , M. Soares-Santos<sup>28</sup> , E. Suchyta<sup>58</sup>, G. Tarle<sup>28</sup> , D. Thomas<sup>13</sup> , C. To<sup>49</sup>,  
 D. L. Tucker<sup>27</sup> , and T. N. Varga<sup>59,60</sup>

(DES Collaboration)

<sup>1</sup> Department of Physics, Duke University, Durham, NC 27708, USA; [rcc29@duke.edu](mailto:rcc29@duke.edu)<sup>2</sup> Department of Physics, University of Arizona, Tucson, AZ 85721, USA<sup>3</sup> Kavli Institute for Particle Astrophysics & Cosmology, P. O. Box 2450, Stanford University, Stanford, CA 94305, USA<sup>4</sup> SLAC National Accelerator Laboratory, Menlo Park, CA 94025, USA<sup>5</sup> Department of Astronomy and Astrophysics, University of Chicago, Chicago, IL 60637, USA<sup>6</sup> Kavli Institute for Cosmological Physics, University of Chicago, Chicago, IL 60637, USA<sup>7</sup> School of Mathematics and Physics, University of Queensland, Brisbane, QLD 4072, Australia<sup>8</sup> The Research School of Astronomy and Astrophysics, Australian National University, ACT 2601, Australia<sup>9</sup> NASA Einstein Fellow<sup>10</sup> Center for Astrophysics | Harvard & Smithsonian, 60 Garden Street, Cambridge, MA 02138, USA<sup>11</sup> Institut d'Estudis Espacials de Catalunya (IEEC), E-08034 Barcelona, Spain<sup>12</sup> Institute of Space Sciences (ICE, CSIC), Campus UAB, Carrer de Can Magrans, s/n, E-08193 Barcelona, Spain<sup>13</sup> Institute of Cosmology and Gravitation, University of Portsmouth, Portsmouth, PO1 3FX, UK<sup>14</sup> School of Physics and Astronomy, University of Southampton, Southampton, SO17 1BJ, UK<sup>15</sup> Centre for Gravitational Astrophysics, College of Science, The Australian National University, ACT 2601, Australia<sup>16</sup> Centre for Astrophysics & Supercomputing, Swinburne University of Technology, Victoria 3122, Australia<sup>17</sup> Department of Physics and Astronomy, University of Pennsylvania, Philadelphia, PA 19104, USA<sup>18</sup> Centro de Investigaciones Energéticas, Medioambientales y Tecnológicas (CIEMAT), Madrid, Spain<sup>19</sup> Jodrell Bank Center for Astrophysics, School of Physics and Astronomy, University of Manchester, Oxford Road, Manchester, M13 9PL, UK<sup>20</sup> University of Nottingham, School of Physics and Astronomy, Nottingham, NG7 2RD, UK<sup>21</sup> Australian Astronomical Optics, Macquarie University, North Ryde, NSW 2113, Australia<sup>22</sup> Lowell Observatory, 1400 Mars Hill Rd, Flagstaff, AZ 86001, USA<sup>23</sup> Sydney Institute for Astronomy, School of Physics, A28, The University of Sydney, NSW 2006, Australia<sup>24</sup> Laboratoire de physique des 2 infinis Irène Joliot-Curie, CNRS Université Paris-Saclay, Bât. 100, Faculté des sciences, F-91405 Orsay Cedex, France<sup>25</sup> Cerro Tololo Inter-American Observatory, NSF's National Optical-Infrared Astronomy Research Laboratory, Casilla 603, La Serena, Chile<sup>26</sup> Laboratório Interinstitucional de e-Astronomia—LIneA, Rua Gal. José Cristino 77, Rio de Janeiro, RJ—20921-400, Brazil<sup>27</sup> Fermi National Accelerator Laboratory, P. O. Box 500, Batavia, IL 60510, USA<sup>28</sup> Department of Physics, University of Michigan, Ann Arbor, MI 48109, USA<sup>29</sup> CNRS, UMR 7095, Institut d'Astrophysique de Paris, F-75014, Paris, France<sup>30</sup> Sorbonne Universités, UPMC Univ Paris 06, UMR 7095, Institut d'Astrophysique de Paris, F-75014, Paris, France<sup>31</sup> Faculty of Physics, Ludwig-Maximilians-Universität, Scheinerstr. 1, D-81679 Munich, Germany<sup>32</sup> Department of Physics & Astronomy, University College London, Gower Street, London, WC1E 6BT, UK<sup>33</sup> Instituto de Astrofísica de Canarias, E-38205 La Laguna, Tenerife, Spain<sup>34</sup> Universidad de La Laguna, Dpto. Astrofísica, E-38206 La Laguna, Tenerife, Spain<sup>35</sup> Center for Astrophysical Surveys, National Center for Supercomputing Applications, 1205 West Clark St., Urbana, IL 61801, USA<sup>36</sup> Department of Astronomy, University of Illinois at Urbana-Champaign, 1002 W. Green Street, Urbana, IL 61801, USA<sup>37</sup> Institut de Física d'Altes Energies (IFAE), The Barcelona Institute of Science and Technology, Campus UAB, E-08193 Bellaterra (Barcelona) Spain<sup>38</sup> Physics Department, William Jewell College, Liberty, MO 64068, USA<sup>39</sup> Astronomy Unit, Department of Physics, University of Trieste, via Tiepolo 11, I-34131 Trieste, Italy<sup>40</sup> INAF-Osservatorio Astronomico di Trieste, via G. B. Tiepolo 11, I-34143 Trieste, Italy<sup>41</sup> Institute for Fundamental Physics of the Universe, Via Beirut 2, I-34014 Trieste, Italy<sup>42</sup> Observatório Nacional, Rua Gal. José Cristino 77, Rio de Janeiro, RJ—20921-400, Brazil<sup>43</sup> Hamburger Sternwarte, Universität Hamburg, Gojenbergsweg 112, D-21029 Hamburg, Germany<sup>44</sup> Department of Physics, IIT Hyderabad, Kandi, Telangana 502285, India<sup>45</sup> Santa Cruz Institute for Particle Physics, Santa Cruz, CA 95064, USA<sup>46</sup> Institute of Theoretical Astrophysics, University of Oslo. P.O. Box 1029 Blindern, NO-0315 Oslo, Norway<sup>47</sup> Instituto de Física Teórica UAM/CSIC, Universidad Autónoma de Madrid, E-28049 Madrid, Spain<sup>48</sup> Excellence Cluster Origins, Boltzmannstr. 2, D-85748 Garching, Germany<sup>49</sup> Center for Cosmology and Astro-Particle Physics, The Ohio State University, Columbus, OH 43210, USA<sup>50</sup> Department of Physics, The Ohio State University, Columbus, OH 43210, USA<sup>51</sup> Departamento de Física Matemática, Instituto de Física, Universidade de São Paulo, CP 66318, São Paulo, SP, 05314-970, Brazil<sup>52</sup> Institut de Física d'Altes Energies (IFAE), The Barcelona Institute of Science and Technology, Campus UAB, E-08010 Barcelona, Spain<sup>53</sup> Physics Department, 2320 Chamberlin Hall, University of Wisconsin-Madison, 1150 University Avenue Madison, WI 53706-1390, USA<sup>54</sup> Department of Astronomy, University of California, Berkeley, 501 Campbell Hall, Berkeley, CA 94720, USA

<sup>55</sup> Institute of Astronomy, University of Cambridge, Madingley Road, Cambridge CB3 0HA, UK

<sup>56</sup> Department of Astrophysical Sciences, Princeton University, Peyton Hall, Princeton, NJ 08544, USA

<sup>57</sup> Department of Physics and Astronomy, Pevensey Building, University of Sussex, Brighton, BN1 9QH, UK

<sup>58</sup> Computer Science and Mathematics Division, Oak Ridge National Laboratory, Oak Ridge, TN 37831, USA

<sup>59</sup> Max Planck Institute for Extraterrestrial Physics, Giessenbachstrasse, D-85748 Garching, Germany

<sup>60</sup> Universitäts-Sternwarte, Fakultät für Physik, Ludwig-Maximilians Universität München, Scheinerstr. 1, D-81679 München, Germany

Received 2022 February 21; revised 2022 July 27; accepted 2022 August 18; published 2022 October 13

## Abstract

Current and future cosmological analyses with Type Ia supernovae (SNe Ia) face three critical challenges: (i) measuring the redshifts from the SNe or their host galaxies; (ii) classifying the SNe without spectra; and (iii) accounting for correlations between the properties of SNe Ia and their host galaxies. We present here a novel approach that addresses each of these challenges. In the context of the Dark Energy Survey (DES), we analyze an SN Ia sample with host galaxies in the redMaGiC galaxy catalog, a selection of luminous red galaxies. redMaGiC photo- $z$  estimates are expected to be accurate to  $\sigma_{\Delta z/(1+z)} \sim 0.02$ . The DES-5YR photometrically classified SN Ia sample contains approximately 1600 SNe, and 125 of these SNe are in redMaGiC galaxies. We demonstrate that redMaGiC galaxies almost exclusively host SNe Ia, reducing concerns relating to classification uncertainties. With this subsample, we find similar Hubble scatter (to within  $\sim 0.01$  mag) using photometric redshifts in place of spectroscopic redshifts. With detailed simulations, we show that the bias due to using redMaGiC photo- $z$ s on the measurement of the dark energy equation of state  $w$  is up to  $\Delta w \sim 0.01$ – $0.02$ . With real data, we measure a difference in  $w$  when using the redMaGiC photo- $z$ s versus the spec- $z$ s of  $\Delta w = 0.005$ . Finally, we discuss how SNe in redMaGiC galaxies appear to comprise a more standardizable population, due to a weaker relation between color and luminosity ( $\beta$ ) compared to the DES-3YR population by  $\sim 5\sigma$ . These results establish the feasibility of performing redMaGiC SN cosmology with photometric survey data in the absence of spectroscopic data.

*Unified Astronomy Thesaurus concepts:* [Cosmology \(343\)](#); [Type Ia supernovae \(1728\)](#)

## 1. Introduction

Type Ia supernovae (SNe Ia) remain a critical tool as standardizable candles for measuring cosmological parameters and constraining models for dark energy. Over the next decade, multiple surveys, such as the Vera Rubin Observatory Legacy Survey of Space and Time (LSST; Ivezić et al. 2019) and the Nancy Grace Roman Space Telescope (Roman; Hounsell et al. 2018; Dore et al. 2019), will discover more than a million SNe, which will be leveraged to make more precise measurements of the dark energy equation-of-state parameter ( $w$ ) and its dependence on cosmic time. The success of these programs will require (i) information about the SN types and (ii) accurate determinations of redshifts. The primary cosmological results from SN surveys have historically been reliant on spectroscopic information, including the first results from the Dark Energy Survey (DES-3YR; Abbott et al. 2019), which were obtained from a sample of 207 spectroscopically confirmed SNe Ia with available host galaxy or SN redshifts. For totals of SNe approaching 2.4 million (the LSST Dark Energy Science Collaboration et al. 2018; C. Frohmaier et al. 2022, in preparation), it will be impossible to spectroscopically observe each SN, due to cost and time constraints. We present here a first implementation of a solution to this problem, by focusing on a sample of SNe Ia in a subset of galaxies where the SN type and redshift can be more easily determined than in the general population.

For the photometric classification of the SNe, recent analyses have made significant progress in rejecting core-collapse SNe (SNe Ibc and II) and selecting samples that are  $>90\%$  pure. The Photometric LSST Astronomical Time-series

Classification Challenge (PLAsTiCC; the PLAsTiCC Team et al. 2018) included a mix of 18 transient models (Kessler et al. 2019), and the top-performing light-curve classifiers achieved 95% levels of purity, by training on a subset of the data (Hložek et al. 2020). SuperNNova (SNN; Moller & de Boissière 2020), a neural net classifier trained on simulations that use PLAsTiCC models (SNIa, SNIax, SNIa-91bg, SNIi, and SNIb/c), has a predicted efficiency from DES simulations of 97.7%–99.5% (Vincenzi et al. 2022; Möller et al. 2022). An alternate approach to photometric classification is to use host galaxy information to avoid problems with low signal-to-noise ratio (S/N) data and sparse sampling. Foley & Mandel (2013) found that galaxy morphology provides the most discriminating information for determining an SN Ia classification probability. Core-collapse SNe have massive ( $>8 M_{\odot}$ ) star progenitors, consistent with observations that they explode almost exclusively in gas-rich star-forming galaxies, whereas SNe Ia have white-dwarf progenitors and appear in a variety of host galaxy types.

To precisely measure redshifts, large-area surveys such as DES (Abbott et al. 2019) and Pan-STARRS1 (PS1; Chambers et al. 2016) have pursued dedicated host galaxy follow-up programs. PS1 used the MMT Observatory and AAOmega spectrograph on the Anglo-Australian Telescope (AAT) to measure spectroscopic redshifts after the survey was completed. DES had a concurrent program (OzDES; Lidman et al. 2020) to measure redshifts during the survey. OzDES also used the AAOmega spectrograph on the AAT, as the Two Degree Field system (2dF) + AAOmega has a similar field of view to the Dark Energy Camera (DECam). However, this approach to obtaining redshifts requires large amounts of dedicated telescope time and additional modeling of spectroscopic efficiency, due to biases toward brighter host galaxies (Vincenzi et al. 2021).

So far, there have been limited studies on using photometric redshift estimates (photo- $z$ ) in a cosmological study with SNe



Original content from this work may be used under the terms of the [Creative Commons Attribution 4.0 licence](#). Any further distribution of this work must maintain attribution to the author(s) and the title of the work, journal citation and DOI.

Ia. Kessler et al. (2010) produced LSST simulations and showed that a light-curve fit using a host galaxy photo- $z$  prior yields comparable redshift precision to spectroscopic redshifts. However, Sako et al. (2011) found that using SN-only photo- $z$ s with real Sloan Digital Sky Survey data resulted in pathologies that propagated to biases in the distances, and therefore to the measurements of cosmological parameters. Other studies (Wojtak et al. 2015; Davis et al. 2019) have found that systematic redshift errors as small as  $10^{-4}$  can mimic a 1% perturbation in  $w$ , but also illustrate that the impact of redshift biases diminishes with increasing redshift.

For SN Ia samples with diverse host galaxy types, the issue of preferentially targeting brighter galaxies is particularly problematic, because there is a correlation between the mass and rest-frame U–R color of the galaxies and the luminosity of the SNe (Kelly et al. 2010; Sullivan et al. 2010; Kelsey et al. 2021). There have also been observed correlations between other global host galaxy properties, such as metallicity and morphological type (Hamuy et al. 2000; Kelly et al. 2010; Smith et al. 2020b), as well as local host galaxy environments (Rigault et al. 2013, 2015; Roman et al. 2018; Rigault et al. 2020; Kelsey et al. 2021). These correlations are not well understood and are the subject of ongoing efforts to implement better bias corrections and modeling (Rigault et al. 2020; Smith et al. 2020b; Brout & Scolnic 2021; Popovic et al. 2021). Since the measurement of  $w$  is based on a relative measurement between distances of SNe at high and low redshift, a redshift-dependent selection of galaxy type may cause a significant systematic in measurements of  $w$ .

Here, we investigate a solution to the above problems by exploiting SNe located in luminous red galaxies (LRGs), which are a well-known homogeneous population consisting of so-called “red and dead” elliptical galaxies. LRGs are expected to contain very low rates of core-collapse SNe, as core-collapse progenitors are massive and largely present in active star-forming galaxies, such as spiral galaxies. Foley & Mandel (2013) found that 98% of all SNe with elliptical host galaxies in the Lick Observatory Supernova Search sample (Leaman et al. 2011) are SNe Ia, implying that host galaxy information alone can reduce photometric contamination from core-collapse SNe, and Irani et al. (2022) conclude that only  $0.3\%_{-0.1}^{+0.3}$  of all core-collapse SNe have elliptical hosts. Second, LRG spectra contain a prominent 4000 Å break, which enables precise and accurate photo- $z$  estimates that have traditionally been utilized in large-scale structure studies. The photo- $z$  bias of these galaxies can be further constrained with the use of red galaxies selected using the red-sequence Matched-filter Galaxy (redMaGiC) algorithm described in Rozo et al. (2016), which utilizes a modified photo- $z$  estimator based on a full red-sequence model. Lastly, limiting the host galaxy type allows for a more consistent sample across redshifts, which is less sensitive to complicated correlations between SN light-curve properties and host galaxy properties. Although in the future enough low-redshift SNe will be observed in LRGs to have an SN sample solely from one host galaxy type, this study instead combines SNe in LRGs at  $z > 0.05$  with the traditional spectroscopic low-redshift sample, to provide an SN sample large enough for Ia cosmological analysis.

Less than 10% of SN host galaxies are expected to be LRGs (Foley & Mandel 2013). For DES, which has 3627 SNe Ia before light-curve quality cuts, and 1606 after quality cuts, this LRG selection yields 227 SNe before cuts and 125 after cuts

(6.26% and 7.78% respectively). For the LSST sample of  $\sim 2$  million SNe, we expect  $\sim 10^5$  SNe to be in LRGs.

In this paper, we provide a first investigation into the feasibility of using photometric redshifts from the redMaGiC galaxy catalog in an SNe Ia cosmology analysis. The outline of the paper is as follows. In Section 2, we summarize the DES SN and host galaxy data used for this work. In Section 3, we discuss the simulations used to validate the method and for estimating bias corrections. In Section 4, we discuss the application of the method to DES-5YR data. In Section 5, we discuss the implications and results of our study. In Section 6, we present our conclusions.

## 2. Data

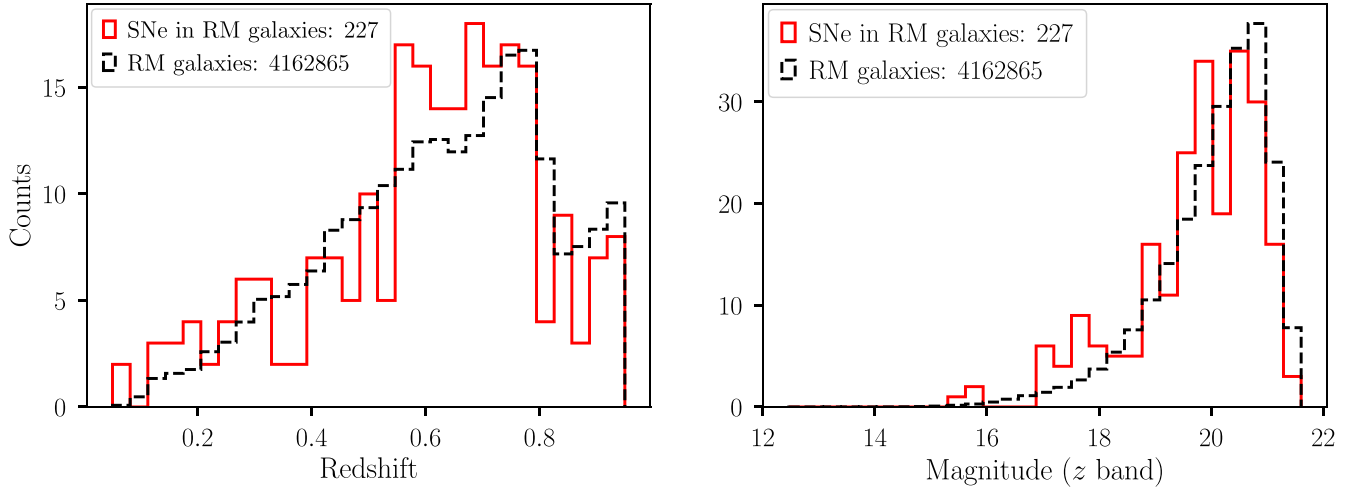
### 2.1. redMaGiC Galaxies

LRGs occupy a very narrow range in color and intrinsic luminosity, and they contain old, red stellar populations. LRGs are a useful probe for large-scale structure studies (Stoughton et al. 2002), as they are intrinsically luminous and therefore can be observed out to high redshift, plus they are relatively massive and therefore tend to cluster strongly. LRG spectral energy distributions (SEDs) have a prominent 4000 Å feature caused by absorption lines from metals in stellar atmospheres, which make LRGs ideal candidates for photo- $z$  estimations.

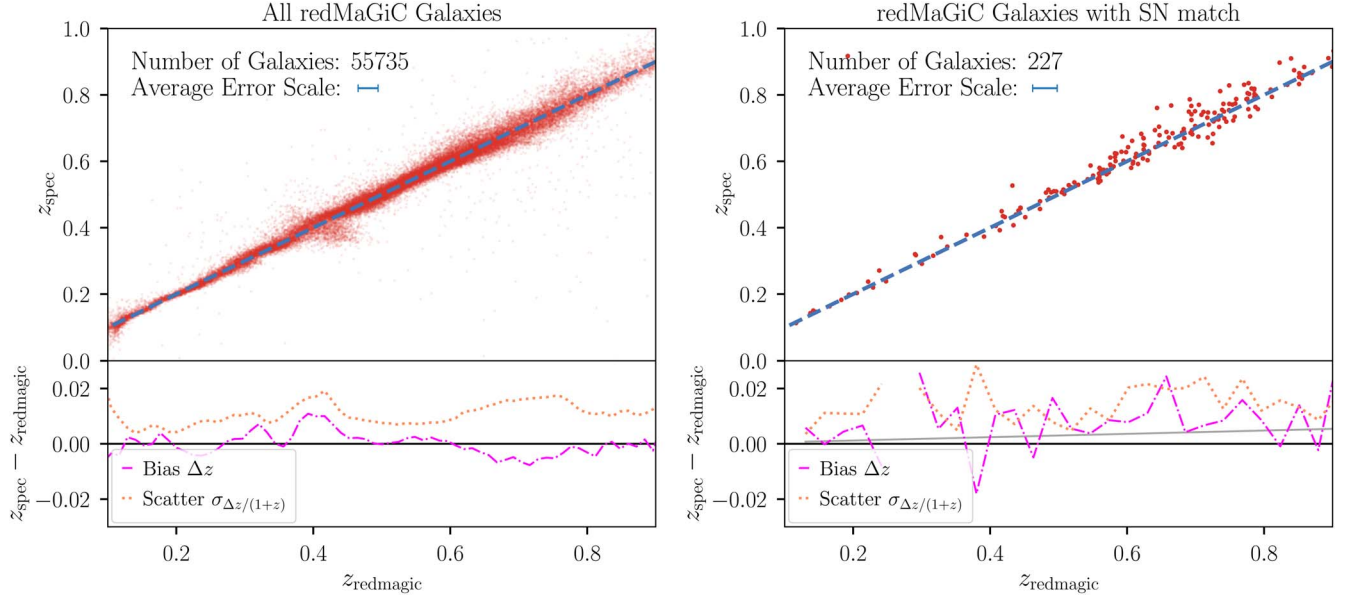
The red-galaxy and photo- $z$  data used in this study were obtained using the redMaGiC algorithm (Roza et al. 2016), run on six seasons of DES data with preliminary photometry. The algorithm is based on the infrastructure of redMaPPer (Rykoff et al. 2014), a red-sequence cluster finder designed for large photometric surveys. redMaPPer characterizes the colors of a red-sequence model as functions of magnitude and redshift. The redMaGiC algorithm can then select red galaxies based on a chosen comoving space density and luminosity threshold. First, redMaGiC fits every red-sequence galaxy with the redMaPPer red-sequence template and computes its best-fit photo- $z$ . Using this photo- $z$ , it computes the galaxy luminosity. Lastly, it applies selection requirements (cuts) to the luminosity and  $\chi^2$  of the template fit, with the cuts being tuned to select a desired comoving space density. As only  $\sim 20\%$  of redMaGiC galaxies are in redMaPPer clusters, we note that it is a fundamental assumption of this selection that red galaxies are a homogeneous population, regardless of their cluster membership.

After applying the redMaGiC cuts, a subset of the selected galaxies with spectroscopic redshifts can be used to further train and validate a photo- $z$  afterburner. To avoid biased selection from using galaxies with spectroscopic follow-up, the redshift calibration uses redMaPPer photometric cluster redshifts ( $z_{\text{cluster}}$ ) for the subset of redMaGiC galaxies that are members of redMaPPer clusters, where each  $z_{\text{cluster}}$  is fit simultaneously with all cluster members and is therefore more accurate than any individual galaxy redshift. The training sample’s median redshift offset  $z_{\text{cluster}} - z_{\text{red}}$  is calculated in bins of  $z_{\text{red}}$ , where  $z_{\text{cluster}}$  is the cluster redshift and  $z_{\text{red}}$  is the initial photometric redshift. This median offset is added to  $z_{\text{red}}$  using spline interpolation, to give the final photometric redshift,  $z_{\text{redmagic}}$ .

The redshift range of the sample is  $z_{\text{redmagic}} \in [0.05, 0.95]$ , and is shown in Figure 1, along with the  $z$ -band magnitude ( $m_z$ ) distribution. The redshift distribution peaks around  $z = 0.7$  and the magnitude distribution peaks around  $m_z = 21.0$ . The redMaGiC algorithm is typically run to produce two sets of



**Figure 1.** Left: the distribution of the redMaGiC (RM) photometric redshifts for all redMaGiC galaxies (dashed black line) compared to the subset with a matched SN (solid red line). Right: the distribution of the  $z$ -band magnitudes for all redMaGiC (RM) galaxies (dashed black line) compared to the subset with a matched SN (solid red line). The histograms for all the RM galaxies are scaled to match the sums of the RM galaxies that host SNe.



**Figure 2.** Top left: photometric redshifts vs. spectroscopic redshifts of the redMaGiC galaxies. The dashed line has a slope of 1 for visual comparison. Bottom left: the dashed-dotted pink line shows the bias (binned  $\overline{\Delta z}$ ) and the dotted yellow line shows the scatter for the redMaGiC photo- $z$ . Only galaxies with a spectroscopic redshift are included in the bias and scatter calculations. Right: the same as the left panels, but for the subset of redMaGiC galaxies with an SN match. A bias of  $0.006z$  is shown in gray in the bottom panel.

catalogs: “high-luminosity” and “high-density.” The high-luminosity catalog restricts the selection to galaxies with luminosity greater than  $1 L_*$  (as defined in Rykoff et al. 2016), to extend to the highest redshift possible. The high-density catalog requires a density of  $\sim 10^{-3} \text{ Mpc}^{-3}$  with a luminosity threshold at  $0.5 L_*$ . To use the largest possible selection of galaxies, we combine the two catalogs to create our catalog of redMaGiC galaxies. To compare the performance of the spectroscopic redshifts ( $z_{\text{spec}}$ ) and  $z_{\text{redmagic}}$ , we select galaxies with an available spectroscopic redshift, which reduces the number of galaxies from 4,162,865 to 55,735.

To quantify the performance of the photometric redshifts, the photo- $z$  bias  $\overline{\Delta z}$  is defined as the median of the offsets  $\Delta z = z_{\text{spec}} - z_{\text{redmagic}}$ , and the photo- $z$  scatter  $\sigma_{\Delta z/(1+z)}$  is defined as  $1.4826 \times \text{MAD}$ , where MAD is the median absolute deviation  $|\Delta z - \overline{\Delta z}|/(1 + z_{\text{spec}})$ . Figure 2 shows the photo- $z$

performance of the combined high-density and high-luminosity year six redMaGiC sample. A comparison of the one-to-one relation between spec- $z$  and photo- $z$  can be seen in the top panels of Figure 2. The bottom halves of the plots show the bias and scatter plotted as a function of  $z_{\text{redmagic}}$ . In the left plot, the full redMaGiC sample has a scatter of less than 0.02 and bias less than 0.01 over the entire redshift interval.

## 2.2. DES SN Data

In this analysis, we use data from the DES SN program (DES-SN) obtained with the DECam (Flaugher et al. 2015) mounted on the 4 meter Blanco telescope at the Cerro Tololo Inter-American Observatory. DES-SN operated over five seasons, taking observations in the optical  $griz$  filters in ten 3 square degree fields at a cadence of  $\sim 7$  days. These images were preprocessed by the DES Data Management team

(Morganson et al. 2018). Next, transients were detected in these images using the Difference Imaging pipeline (DIFFIMG; Kessler et al. 2015), by subtracting reference images from the new observations. While scene modeling photometry (Holtzman et al. 2008; Astier et al. 2013; Brout et al. 2019b) is planned for the entire DES-5YR photometric sample, we utilize DIFFIMG photometry that is calibrated at the 2% level. This precision is sufficient for the purposes of this redMaGiC analysis, as calibration errors have the same effects on distances for spec- $z$  and photo- $z$ , and here we only report differences between these two analyses. The transient sample is defined after restricting the candidates to those with at least two detections at the same location on two separate nights in any band and that pass an automated artifact rejection algorithm (AUTOSCAN; Goldstein et al. 2015). From these criteria, approximately 30,000 transients are identified, which include SNe, active galactic nuclei, and other transients and artifacts.

For each transient, a host galaxy is assigned using the directional light radius method (Sullivan et al. 2006; Gupta et al. 2016; Popovic et al. 2020). This host matching is performed with the depth-optimized coadds from Wiseman et al. (2020). The Photometric Supernova IDentification software (Sako et al. 2011) was run during survey operations on every active candidate, which fit the transient light curve, to provide an estimate of the time of peak brightness, and provided preliminary classifications. This information helped to inform the targeting for the host galaxy follow-up spectroscopic program (Smith et al. 2020a), by eliminating non-SN transients.

The DES-5YR SN-like photometric sample is restricted to SNe with associated host galaxy spectroscopic redshifts. These redshifts are obtained from the spectroscopic follow-up (Smith et al. 2020a) program, primarily from the OzDES survey (Yuan et al. 2015; Childress et al. 2017; Lidman et al. 2020). OzDES is a 100-night program using the 2dF+AAOmega spectrograph on the 3.9 meter AAT. External redshift catalogs from the literature (as cited in Table 1 of Vincenzi et al. 2021) are used to supplement and optimize this redshift information. Following OzDES selection cuts and host associations, we have 5049 galaxies with secure redshifts.

We further restrict the DES-5YR photometric sample (with no classifiers applied) to SNe that have redMaGiC host galaxies. To associate the host galaxies, we find all SNe with DLR-assigned host galaxy RA/Dec coordinates matching within 1 arcsecond to a redMaGiC galaxy from the year six run. 227 SNe, approximately 6% of the  $\sim 3700$  SNe fit by SALT2 in the 5YR sample, have redMaGiC host galaxies. The right side of Figure 2 shows the redshift performance for the subset of redMaGiC galaxies with an SN match. The median redshift bias for the redMaGiC SNe is  $\Delta z = 0.008$ , and we find a redshift-dependent trend of  $\sim 0.006z$ , which we show in Figure 2. We average the bias measured across 100 random samples of 227 galaxies drawn from the full redMaGiC distribution to obtain a mean bias of 0.001, with a scatter of 0.001, implying that the mean bias for the redMaGiC SNe is a  $>5\sigma$  fluctuation from the full redMaGiC sample bias. As it is therefore possible that the subpopulation of redMaGiC SNe has an unmodeled selection effect, we propagate the  $\sim 0.006z$  bias as a systematic in Section 4.2.2. The mean scatter for the subsample is 0.015, compared to 0.012 for the full sample, and 0.015 from the averaged same-size samples.

**Table 1**  
Summary Table of the Post-SALT2 Fit Cuts

Post-SALT2 Fit Cut	Number Remaining	Number Rejected
SNe in redMaGiC galaxies fit by SALT2	224	
SN color $ c  < 0.3$	185	39
SN color uncertainty $\sigma_c < 0.2$	184	1
SN stretch $ x_1  < 3.0$	147	37
SN stretch uncertainty $\sigma_{x_1} < 1.0$	125	22
SN $t_0$ uncertainty $\sigma_{t_0} < 2.0$	125	0
Milky Way color excess $E(B - V) < 0.3$	125	0

In addition to the DES-SN sample, we include an external spectroscopically confirmed low-redshift sample to anchor the Hubble diagram. We use 182 SNe Ia from the Foundation Supernova Survey (Foley et al. 2018; Jones et al. 2018). We note that this low-redshift sample contains SNe from a range of host galaxy types.

### 2.3. Light-curve Fits, Distance Estimation, and Cosmological Parameter Recovery

We use the SALT2 light-curve model (Guy et al. 2007, 2010) to fit SN light curves and standardize the SN Ia brightnesses. This fitting is implemented in the SuperNova ANALysis software (SNANA; Kessler et al. 2009b) framework, based on the MINUIT  $\chi^2$  minimization algorithm, to obtain best-fit parameters and uncertainties. The fitted parameters are color  $c$ , stretch  $x_1$ , epoch of SN peak brightness  $t_0$ , and overall amplitude  $x_0$ , with  $m_B = -2.5 \log_{10}(x_0)$ . The distance modulus,  $\mu$ , is estimated using the Tripp estimator (Tripp 1998; Astier et al. 2006):

$$\mu = m_B + \alpha x_1 - \beta c - M_{z_i} + \delta\mu_{\text{bias}}, \quad (1)$$

where  $M_{z_i}$  is the distance offset in redshift bins  $z_i$ ,  $\alpha$  and  $\beta$  are coefficients parameterizing the relationship between stretch, color, and luminosity, and  $\delta\mu_{\text{bias}}$  is the distance bias correction, which is described below. Rather than fitting for nuisance parameters ( $\alpha$ ,  $\beta$ ) in a global fit, we use values measured by the DES (Brout et al. 2019a);  $\alpha = 0.145$ ,  $\beta = 3.1$ .

Before fitting with SALT2, the data are further restricted to transients that have at least two bands with data satisfying a maximum  $S/N > 4$ . After fitting with SALT2, we apply the following selection requirements that are typical for a cosmology analysis, along with an additional color uncertainty requirement:

1. fitted color  $|c| < 0.3$ ;
2. fitted color uncertainty  $\sigma_c < 0.2$ ;
3. fitted stretch  $|x_1| < 3.0$ ;
4. fitted stretch uncertainty  $\sigma_{x_1} < 1.0$ ;
5. fitted  $t_0$  uncertainty  $\sigma_{t_0} < 2.0$  days; and
6. Milky Way color excess  $E(B - V) < 0.3$ .

In Table 1, we show the number of SNe remaining after each fit cut. Using the Beams with Bias Corrections (BBC; Kessler & Scolnic 2017) formalism, we bias correct our distance

modulus values. The simulations used to determine bias corrections (biascor) are detailed in Section 3. Typical cosmological Ia analyses use higher-dimensional bias corrections (BBC5D/BBC7D/BBC-BS20; Popovic et al. 2021), with biases binned along SN properties, and use simulations with a  $2 \times 2$  grid of  $\alpha$  and  $\beta$  (to interpolate for each fitted  $\alpha$ ,  $\beta$ ). However, to simplify this first redMaGiC analysis, we use redshift-dependent (1D) bias corrections with no dependence on other parameters, and our simulations have fixed  $\alpha$  and  $\beta$ . The BBC fit determines an intrinsic scatter term ( $\sigma_{\text{int}}$ ) and  $M_{z_i}$  in  $N_z$  BBC redshift bins. From the SALT2- and BBC-fitted parameters, we compute a bias-corrected distance (Equation (1)) for each SN to use in the cosmology fit.

The uncertainty in  $\mu$  is given by:

$$\sigma_{\mu}^2 = \sigma_{\text{int}}^2 + \sigma_{\text{Tripp}}^2 + (\sigma_{\mu}^{\text{pec}})^2 + (\sigma_{\mu}^z)^2, \quad (2)$$

where  $\sigma_{\text{int}}$  is the intrinsic scatter needed to achieve a reduced  $\chi^2$  ( $\chi^2/\text{degree of freedom} = 1$ ) for the BBC fit,  $\sigma_{\text{Tripp}}$  describes the uncertainty computed from the fitted light-curve parameters and their covariances,  $\sigma_{\mu}^{\text{pec}}$  is the contribution from the peculiar velocity uncertainty  $\sigma_{\text{vpec}}$ , with

$$\sigma_{\mu}^{\text{pec}} = \left( \frac{5}{\ln(10)} \right) \frac{1+z}{z(1+z/2)} \left( \frac{\sigma_{\text{vpec}}}{c} \right), \quad (3)$$

and  $\sigma_{\mu}^z$  is the contribution from the redshift uncertainty  $\sigma_z$ .

In Appendix A.1, we explain why the redshift uncertainty ( $\sigma_z$ ) is not included in Equation (3), as it previously had been in Kessler & Scolnic (2017). Instead, an empirical method is used to account for the contribution of the photo- $z$  uncertainties to the uncertainty in  $\mu$  ( $\sigma_{\mu}^z$ ), as explained in Section 4.2.1.

Following recent studies of systematic biases in SN Ia cosmological analyses (Brout et al. 2021; Popovic et al. 2021), we fit for  $w$  using a Gaussian prior on  $\Omega_M$ , of mean 0.311 and  $\sigma = 0.01$ . We use the “wfit”  $\chi^2$  minimization program implemented in SNANA.

### 3. Simulations

To quantify the cosmological biases from using photometric redshifts, we use SNANA catalog-level simulations to realistically represent the DES-5YR photometric SN sample and to analyze it alongside the real data. We exclude core-collapse SN contamination from our simulations, as significant contamination is not expected, as discussed in Section 4.1. In addition, we generate large samples that are used by BBC for determining the bias corrections (Kessler & Scolnic 2017), to correct for the known selection effects in our analysis.

#### 3.1. Baseline DES Simulation

We use the SNANA software with the Pippin pipeline (Hinton & Brout 2020) to produce our simulations. Following the detailed simulations developed in Kessler et al. (2019), we generate realistic transient light curves with several modifications. Briefly, the simulation consists of three major steps. First, a source SED is generated, and various astrophysical effects, such as cosmological dimming, galactic extinction, lensing, and redshift effects, are applied. The SED model is then integrated over the DES filters, and observational noise is added using the DES observing conditions (point-spread function, sky noise, and photometric zeropoints). Last, the detection efficiency and spectroscopic selection functions of

**Table 2**  
Parent Population Parameters, Averaged over Host Galaxy Mass Bins

		Mean	$\sigma_-$	$\sigma_+$
SNe with redMaGiC hosts	$c$	−0.04	0.04	0.13
	$x_1$	−0.86	1.69	1.35
DES-3YR sample	$c$	−0.09	0.02	0.16
	$x_1$	0.15	1.01	0.66

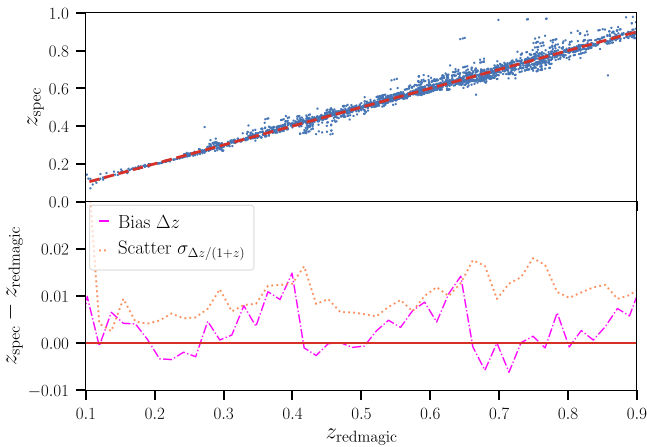
DES are implemented to select simulated events. To describe the SN Ia brightness variation, we vary the SALT2 SED using the G10 intrinsic scatter model from Kessler et al. (2013).

Vincenzi et al. (2021; hereafter, V21) make several improvements to the DES-3YR simulations in order to replicate the DES-5YR photometric SN sample, which contains both core-collapse SNe and SNe Ia, but not other transients. We provide an overview of the important features utilized in our simulations. First, V21 uses a model of the host galaxy spectroscopic redshift efficiency that is parametrized as functions of the host galaxy brightness, color, and year of discovery. V21 also improves on the host galaxy library from Smith et al. (2020b), by compiling galaxy masses and star formation rates (SFRs), and accounting for differing SN rates in different types of galaxies. Simulating SN host galaxies based on published SN rates ensures that the host galaxy property dependencies are appropriately accounted for and that selection effects are modeled accurately across different galaxy types.

#### 3.2. Modifications to the Baseline DES-5YR Simulation

To properly simulate the SN Ia samples, the underlying distributions of the SALT2 parameters  $x_1$  and  $c$  must accurately reproduce our observations. Previous analyses (Scolnic et al. 2018; Abbott et al. 2019) have used the method in Scolnic & Kessler (2016) to determine a migration matrix describing the impact of the selection effects, noise, and intrinsic scatter on the underlying distributions. We use this methodology as implemented in the parent population-fitting program from Popovic et al. (2021) to account for the host galaxy stellar mass relationship. These parent populations are described by an asymmetric Gaussian. In comparison to the population fits for the full DES-3YR spectroscopic sample, we find that the redMaGiC population parameters differ in color and stretch. When averaged over host galaxy mass bins, the subset redMaGiC population is described by the parameters as given in Table 2. We provide the full parent population parameters for both the subset redMaGiC population and the full DES-3YR spectroscopic sample in Appendix A.2. We highlight that the lower value of mean  $x_1$  for the redMaGiC subsample is consistent with previous studies that show that higher-mass galaxies and lower specific star formation rates (sSFRs) are correlated with lower  $x_1$  values (Childress et al. 2014; Rigault et al. 2020; Nicolas et al. 2021).

We modify the V21 host galaxy library and select only passive bright galaxies to mimic the selection of redMaGiC galaxies. Selecting only passive galaxies, as determined by  $\log(\text{sSFR}) < -11.5 \text{ yr}^{-1}$  (Sullivan et al. 2006; V21), we apply a cut on the  $r$ -band magnitude in the host galaxy redshift efficiency map,  $m_r < 23.3$ , and a cut on the host galaxy mass,  $\log \text{Mass} > 10.5$ , based on the distributions for the entire redMaGiC galaxy sample.



**Figure 3.** Redshift bias and scatter, as defined in Figure 2, but for a random selection of 3000 SNe from simulations.

To accurately simulate the photo- $z$  biases and scatter when using photometric redshifts, we include a photo- $z$  for each galaxy in the host galaxy library, based on the bias and scatter from the redMaGiC catalog. For each galaxy in the modified V21 host galaxy library, we find its closest match in redshift to the redMaGiC catalog, evaluate the bias  $z_{\text{redmagic}} - z_{\text{spec}}$  for the redMaGiC galaxy, and add this bias to the host galaxy true redshift value to determine the photo- $z$ . While this galaxy matching would ideally be weighted by mass, to prevent the preferential selection of lower-mass galaxies, we find that the range of masses for redMaGiC host galaxies is narrow (as further discussed in Section 5), circumventing this concern. Figure 3 shows that the photo- $z$  redshift bias and scatter are well reproduced with respect to the data. These photometric redshifts are propagated into the simulated data.

When the color–luminosity relation  $\beta$  is measured from the data, we obtain  $\beta = 2.0$ . We therefore simulate our redMaGiC-hosted SN sample with  $\beta$  of 2.0 as well. However, in the BBC step of the analysis, we fix  $\beta = 3.1$ , as described in Section 2.3, due to the inclusion of the low- $z$  anchor. A summary of the SN and host galaxy simulation properties is given in Table 3.

### 3.3. Comparison with Data

To validate the simulation, we normalize the total number of simulated SNe to the total number of observed SNe, and find that our simulations reproduce the redshift distributions from the data well, as seen in Figure 4. We find that the light-curve parameter ( $c$ ,  $x_1$ ,  $m_B$ ) distributions are also well reproduced. For redshift, we find a reduced  $\chi^2 = 103/30$ . For the light-curve parameters  $c$ ,  $x_1$ , and  $m_B$ , we find  $\chi^2 = 60/30$ ,  $42/30$ , and  $55/30$ , respectively. While the  $\chi^2$  value for redshift is somewhat high, due to the discrepant bins around  $0.3 < z < 0.5$ , the current DES-5YR analysis (Figure 7 in V21) reports a comparable reduced  $\chi^2$  value for the shallow fields of 65/22. There are likely some unmodeled selection and noise effects. We note that the redshift agreement could have been improved if the redMaGiC algorithm had been applied to the host galaxy library, rather than utilizing the rough cuts here, but this is beyond the scope of this work. Notably, the general shape agreement at higher redshift ( $z > 0.55$ ) is of the greatest relevance, as it is where the distance bias correction impact is largest. For  $c$ ,  $x_1$ , and  $m_B$ , our  $\chi^2$  values are also comparable

**Table 3**  
Simulation Inputs and SN Properties

SN Ia Property	
SED model	SALT2.JLA-B14_LAMOPEN
SED variation	G10
$\alpha$	0.15
$\beta$	2.0
Parent Populations	see Table 2
HOSTLIB (V21)	
Host logMass	>10.5
Host $r$ mag	<23.3
Host log(sSFR)	<-11.5 (passive)

to V21, which finds values of 62/22, 29/21, and 37/19, respectively.

To compare the simulated host galaxy photometric redshifts to the data, we examine the mean redshift bias and scatter in the redshift range 0.1–0.9, as illustrated in Figures 2 and 3. The combined high-density and high-luminosity redMaGiC catalog has a mean redshift bias of 0.0005 and a mean redshift-binned scatter of 0.0106, without any outlier cut. A random selection of 3000 simulated host galaxy redshifts has a mean bias of 0.0003 and an rms scatter of 0.0099. Across the redshift bins, the simulated redshifts have a subpercent bias and a scatter of less than 0.02, accurately reproducing the data.

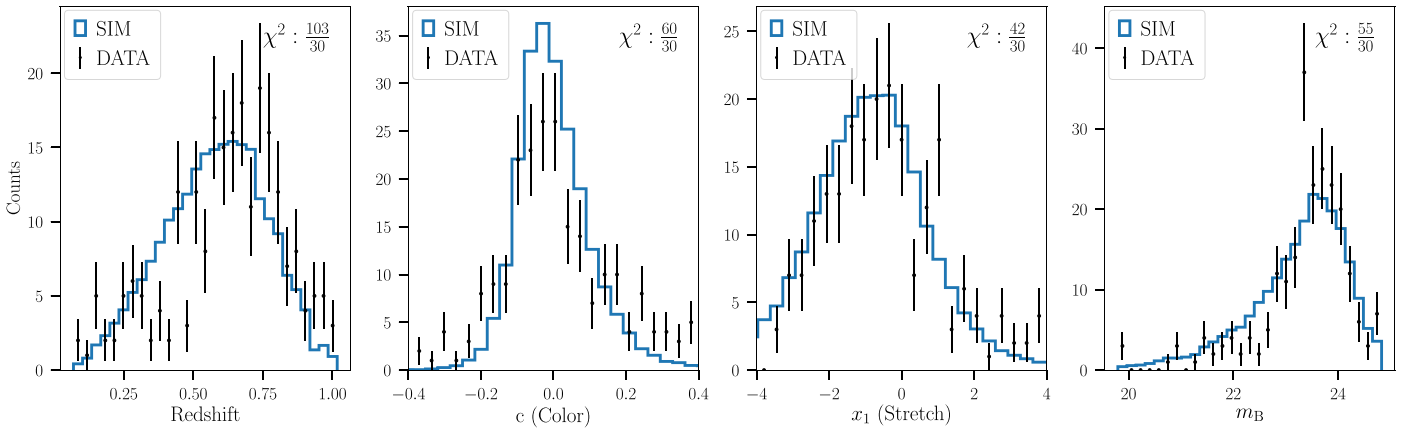
## 4. Analysis and Results

We next discuss the results from our use of redMaGiC photometric redshifts for SN Ia cosmology. In Section 4.1, we quantify and discuss the SN Ia purity for the SNe in redMaGiC galaxies. In Section 4.2, we describe the performance of photo- $z$ s in comparison to spec- $z$ s for our simulations and the effects on cosmological parameters. In Section 4.3, we apply our methods to data and compare the results with our simulations.

### 4.1. Potential Core-collapse Contamination

Large elliptical galaxies such as LRGs are expected to contain mostly SNe Ia (Hakobyan et al. 2020), with very low rates of core-collapse SNe. We quantify the potential core-collapse contamination in our redMaGiC subsample by examining the photometric light-curve classification probabilities. The classification probabilities are obtained with the SNN (Moller & de Boissière 2020) photometric SN classifier trained on the “baseline” DES-like simulation presented in Vincenzi et al. (2022), which is generated from SEDs that include SALT2 and V19 core-collapse templates (Vincenzi et al. 2019). SNN gives a probability ranging from 0 to 1.0, with 1.0 being most-likely-Ia. To consider potential contaminants, we define an unlikely-Ia SN as having a probability of being a Type Ia of  $< 0.5$ . With the conventional SALT2 cosmology cuts (Betoule et al. 2014), the color uncertainty cut as included in this analysis, and no classifier, the simulated DES-5YR photometric SN sample includes 8% contamination (V21; Möller et al. 2022). Of the 125 SNe in redMaGiC galaxies that pass the post-SALT2 fit cuts, four are classified by SNN as unlikely-Ia ( $\sim 3\%$ ).





**Figure 4.** Distributions of redshift (left) and light-curve parameters  $c$  (middle left),  $x_1$  (middle right), and  $m_B$  (right) for the data and simulations. The data are represented by the black points, while the simulations are represented by the blue histograms. The simulation histograms are normalized to the data. The reduced  $\chi^2$  value is reported for each parameter. The covariances between parameters are not shown, as they are found to be small.

For comparison, we consider the SNN classification probabilities for the DES-5YR spectroscopically confirmed SN Ia sample, which serves as a “truth” set of SNe Ia. Of the 401 “true” SNe Ia, three are classified by SNN as non-Ia ( $\sim 1\%$ ). These fractions and percentages are shown in Table 4. We also consider the sample of the DES-5YR spectroscopically confirmed non-Ia SNe and find that there is no overlap with the redMaGiC SN sample.

Of the four events in the redMaGiC subsample that are classified as non-Ia by SNN, one is a spectroscopically confirmed Type Ia, and two are classified as Ia when SNN is instead trained on J17 templates (Jones et al. 2017). The baseline SNN model for DES in Möller et al. (2022) also classifies one of the events as Ia. In particular, we note that using DIFFIMG, the misclassified spectroscopically confirmed SN Ia has inaccurately subtracted template images in the  $g$  band. Notably, photometric classifiers do not have 100% efficiency and can miss true SNe Ia. We confirm the claim that redMaGiC galaxies have very low rates of core-collapse SNe.

#### 4.2. Results from Simulations

We utilize our simulations, as described in Section 3, to characterize the systematic effects of using photometric redshifts to measure  $w$ . Within the SNANA framework, we measure cosmological parameters using both the spectroscopic redshift and the redMaGiC host galaxy photo- $z$ , as described in Section 3.2.

With the resulting light curves, we perform the analysis detailed in Section 2.3 and obtain  $\mu$  for each event. The true distance in each biascor is computed from the measured redshift, either the spec- $z$  or the redMaGiC host galaxy photo- $z$ . While the dispersion of the Hubble residuals will be larger, as a result of using 1D (redshift) bias corrections instead of 5D ( $z$ ,  $x_1$ ,  $c$ ,  $\alpha$ ,  $\beta$ ), we clarify that no additional biases are introduced, because our simulations accurately model the data for each redshift case and therefore produce the appropriate bias correction. We study the impact of using incorrect bias corrections due to the potential mismodeling of redshift bias and scatter in Section 4.2.2. The bias corrections for the anchoring low-redshift sample are computed separately. As mentioned in Section 3, although the DES sample is simulated with  $\beta = 2.0$ , for this study at the BBC step we fix  $\beta = 3.1$ , to remain consistent with the low- $z$  sample. We again clarify that

**Table 4**  
Potential Core-collapse Contamination

	Fraction (%) of SNe Classified by SNN as Unlikely-Ia
Simulated DES-5YR photometric SN sample with no classifier	135/1680 (8%)
SNe in redMaGiC galaxies	4/125 ( $\sim 3\%$ )
DES-5YR spectroscopically confirmed SN Ia sample	3/401 ( $\sim 1\%$ )

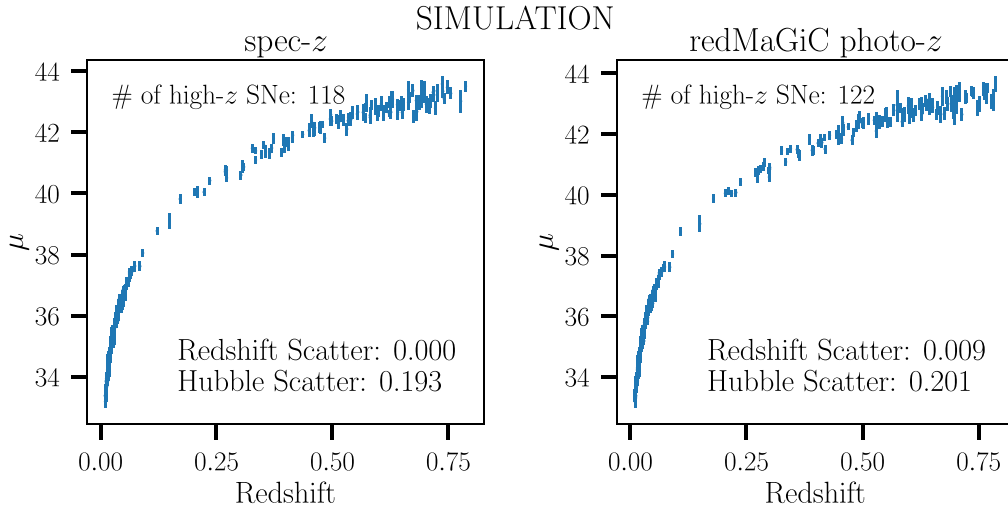
any biases introduced due to the use of samples with different  $\beta$  will be the same when using spectroscopic and photometric redshifts, and therefore will not contribute to the  $\Delta w$  values reported here.

##### 4.2.1. Redshift Contribution to Distance Modulus Uncertainty

To estimate the contribution to the distance modulus uncertainty from the photometric redshift uncertainty, we examine the difference in the Hubble residual scatter between spec- $z$ s and photo- $z$ s using simulations. To avoid statistical limitations from the redMaGiC sample size, we enlarge the host galaxy library, by applying the same photo- $z$  bias as described in Section 3.2, to the V21 host galaxy library, without the redMaGiC-like galaxy cuts. As a cross-check, we also simulate a second set of photo- $z$  using a simple rms map, where the host galaxy photo- $z$  scatter is described as a function of redshift (as seen in Figure 2). We find that for the DES redshift range in both sets of simulations, the distance modulus uncertainty contribution from the use of photo- $z$ s is  $\sim 0.06$  mag, which is small compared to the rms from the distance measurement uncertainty (using the spec- $z$ ) of  $\sim 0.18$  mag or higher. For this work, we therefore neglect this contribution to the uncertainty in  $\mu$ , and note future methods for treating redshift uncertainties in Section 5.

##### 4.2.2. Hubble Diagrams and Cosmological Parameters

Using the spectroscopic and photometric host galaxy redshifts, we analyze the simulated data to produce Hubble diagrams with  $\sim 120$  simulated SNe, shown in Figure 5. The redshift scatter for spectroscopic redshift is by definition 0.00.



**Figure 5.** Hubble diagram from analyzing the simulations for (left) the spec- $z$  from the host galaxy and (right) the redMaGiC photo- $z$ s from the host galaxy. The number of high- $z$  SNe is shown in each panel, as well as the redshift scatter  $\sigma_{\Delta z/(1+z)}$  and Hubble scatter.

**Table 5**  
Redshift and Hubble Scatter for Simulations and Data

Method	Simulation		Data	
	Redshift Scatter $\sigma_{\Delta z/(1+z)}$	Hubble Scatter	Redshift Scatter $\sigma_{\Delta z/(1+z)}$	Hubble Scatter
spec- $z$	0.000	0.193 mag	0.000	0.196 mag
redMaGiC photo- $z$	0.009	0.201 mag	0.014	0.193 mag

We obtain a scatter of 0.009 for the redMaGiC photo- $z$  and compute the Hubble scatter (i.e., the scatter of the Hubble residuals) using a robust measure of the standard deviation, defined as  $1.48 \times \text{MAD}$ . The Hubble scatter for the spec- $z$  case is 0.193 mag, while for the redMaGiC photo- $z$ , the Hubble scatter is 0.201 mag. As expected, both the redshift and Hubble scatter are larger for the redMaGiC photo- $z$  than spec- $z$  (summarized in Table 5). The BBC nuisance parameters (fixed values for  $\alpha$  and  $\beta$  and floated values for the intrinsic scatter  $\sigma_{\text{int}}$ ) are provided in Table 6.

In Table 7, we show  $\Delta w$ ,

$$\Delta w = w_{\text{spec}} - w_{\text{phot}}, \quad (4)$$

the difference in  $w$  between using the spectroscopic redshift and the photo- $z$  method. This difference is averaged over 150 statistically independent simulations to obtain an average  $\Delta w$ . We find

$$\Delta w = -0.0011 \pm 0.0020, \quad (5)$$

with standard deviation 0.0249.

Next, we examine systematic variations in which the simulated photo- $z$  bias or scatter does not match the data. To improve our  $w$ -bias estimate from systematics, we first evaluate the effect of an exaggerated shift, and then assume a linear scale for a more realistic shift. For the photo- $z$  scatter systematic test, a biascor is generated with an analytic description of the host photo- $z$ , where  $z_{\text{phot}} - z_{\text{spec}}$  is drawn from a Gaussian of width  $\sigma = 0.03(1+z)$ . We measure  $\frac{d(\Delta w)}{d(\Delta \text{scatter})} = \frac{0.0107}{0.03}$  and estimate a realistic systematic of 0.0054, given scatter of 0.015. For the photo- $z$  bias systematic test, as mentioned in Section 2, we measure the change in  $w$  with respect to the change in bias. A biascor is generated with

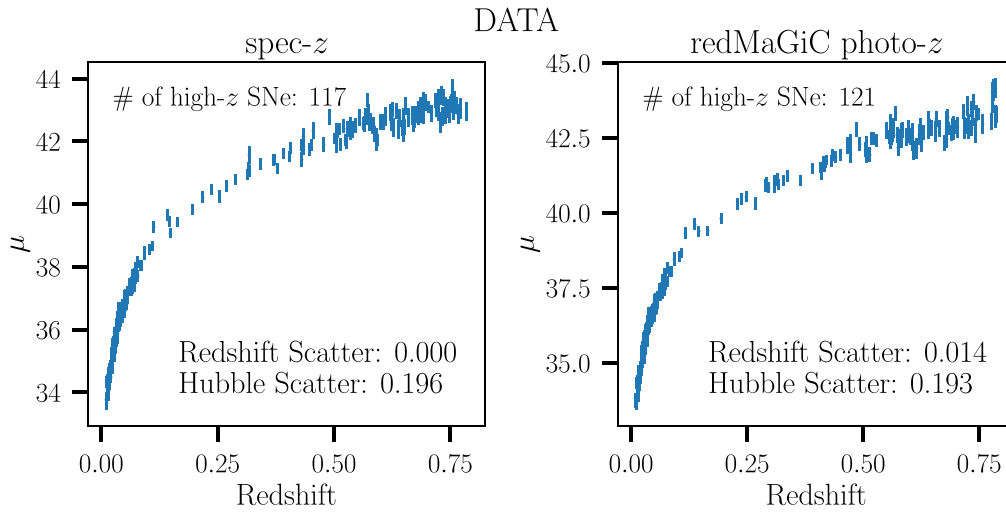
**Table 6**  
BBC Nuisance Parameters for Simulations and Data

Method	Simulation			Data		
	$\alpha$	$\beta$	$\sigma_{\text{int}}$	$\alpha$	$\beta$	$\sigma_{\text{int}}$
spec- $z$	0.14	3.1	0.106	0.14	3.1	0.138
redMaGiC photo- $z$	0.14	3.1	0.111	0.14	3.1	0.145

**Note.**  $\alpha$  and  $\beta$  are fixed, while  $\sigma_{\text{int}}$  is floated.

the host photo- $z$  containing an additional bias of  $0.006z$ . Applying the bias correction to the data, we measure  $\frac{d(\Delta w)}{d(\Delta \text{bias})} = \frac{0.0171}{0.006}$ , and therefore a potential systematic bias of 0.0171.

Without utilizing the actual spectroscopic redshifts of our sample of 227 SNe to ascertain a potential systematic bias, we also consider a realistic test of the potential calibration shifts of the photometric redshifts, as used in current large-scale structure cosmological analyses. We generate a biascor with  $z$ -dependent bias, as determined in the two-parameter fit calibration of the redMaGiC galaxy sample using clustering redshifts, or “cross-correlation redshifts,” as used for DES weak-lensing and galaxy clustering studies. Cawthon et al. (2022) present the best-fit shift and stretch parameters that are applied to the redMaGiC photometric redshift distributions to better match the redshifts determined via angular cross correlation of the redMaGiC sample with spectroscopic galaxy samples. We parameterize this shift (given as  $\Delta z$  in Cawthon et al. 2022, Table 7) as a function of redshift, using cubic spline interpolation, and add it to the photo- $z$  biascor simulated as described in Section 3.2. We find  $\Delta w = -0.0050 \pm 0.0024$ ,



**Figure 6.** Hubble diagrams for the redshift methods as described in Figure 5, but using data. The number of high- $z$  SNe, as well as the redshift scatter  $\sigma_{\Delta z/(1+z)}$  and Hubble scatter, are given for each redshift method.

**Table 7**  
Difference in  $w$  ( $\Delta w$ ) between Photo- $z$  and Spec- $z$

Method	Simulation			Data	
	$\Delta w$	$\Delta w$ Error	$\Delta w$ STD	$\Delta w$	$w$ Uncertainty
spec- $z$	0.00	0.00	0.00	0.00	0.0432
redMaGiC photo- $z$	-0.0011	0.0020	0.0249	0.0049	0.0458
redMaGiC photo- $z$ with additional $z$ -dependent bias biascor	-0.0050	0.0024	0.0294	-0.0146	0.0641

**Note.** The estimated uncertainty in  $w$  for the spectroscopic case is 0.0432 for the data and, on average, 0.0753 for the simulations.

with a standard deviation of 0.0294. These  $\Delta w$  values are also shown in Table 7. While each of these biascor tests results in larger  $\Delta w$ , they remain consistent within the standard deviations. This indicates that the use of redMaGiC photo- $z$  is robust to potential mismodeling in our biascor simulations.

We also test the impact of having removed the  $\sigma_z$  term from Equation (3), as described in Section 2.3 and Appendix A.1. We find  $\Delta w = 0.0098 \pm 0.0029$ , with a standard deviation 0.0361. The mean value of  $\Delta w$  is not strongly impacted, but the uncertainties are increased as expected, due to the overestimated redshift error when  $\sigma_z$  is included.

#### 4.3. Results from Data

The same methods used on the simulations are applied to our data. For bias corrections, we generate biascor simulations, as described in Section 3. Notably, the measured Hubble scatter when using the full redshift range is larger than predicted from the simulations (0.271 mag versus 0.192 mag). This discrepancy is due to the scatter at  $z > 0.8$ , which is 0.451 mag for the data and 0.238 mag for the simulations. This indicates that we are not adequately modeling the SN light curves at higher redshifts. Therefore, we limit the redshift range of our data and simulation samples to  $z < 0.8$ , the upper limit of the redshift range for the DES-3YR spectroscopic sample. We obtain the Hubble diagrams shown in Figure 6 and the  $\Delta w$  for the data shown in Table 7. For redMaGiC photo- $z$ , we obtain a redshift

scatter of 0.014 and a Hubble scatter of 0.193 mag. These figures are summarized in Table 5. We measure intrinsic scatter  $\sigma_{\text{int}} = 0.138$  for the data in comparison to 0.106 for our simulations. Similarly, we measure  $\sigma_{\text{int}} = 0.145$  in comparison to 0.111 for the photo- $z$  case. These floated BBC parameters, along with the fixed values for  $\alpha$  and  $\beta$ , are provided in Table 6.

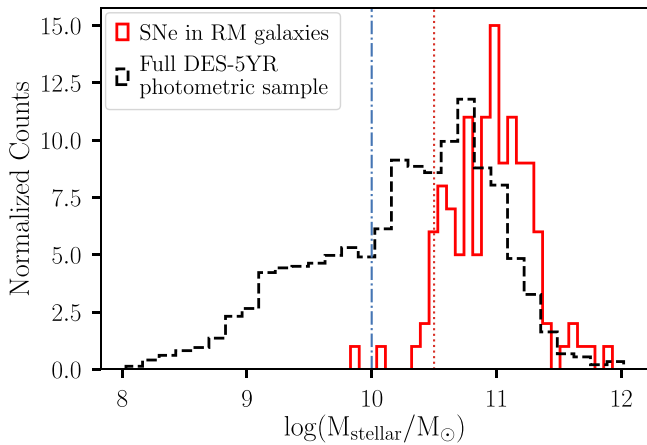
When using redMaGiC photo- $z$ , we obtain

$$\Delta w = 0.0049 \quad (6)$$

compared to the spectroscopic case. This result is consistent with our expectations from simulations ( $-0.0011 \pm 0.0020$ , with a standard deviation of 0.0249), and is significantly smaller than the data  $w$  uncertainty using spec- $z$  (0.0432), indicating that systematic uncertainties from using the redMaGiC photo- $z$  are subdominant to our overall  $w$  uncertainty. In summary, and as expected from the simulations, replacing spectroscopic redshifts with photometric redshifts has a negligible impact on the width of the cosmological posteriors. Moreover, the systematic shift in the posterior is negligible compared to the width of the posterior.

## 5. Discussion

There are three advantages to a redMaGiC-only SN analysis: (i) the lower probability of having non-Ia SNe; (ii) the ability to



**Figure 7.** LogMass distribution for the full DES-5YR photometric sample (dashed black line) and for the subsample of SNe with redMaGiC host galaxies (solid red line). The full DES-5YR sample is normalized to the redMaGiC subsample. The red dotted line at a logMass of 10.5 indicates the cut made for the simulated host galaxy library. The blue dashed-dotted line indicates the cutoff typically applied to measure the mass step.

use host galaxy photo- $z$ ; and (iii) the robustness of the SN host galaxy correlations. The first two of these have been covered extensively in this paper, so we here address the third. We note that of our redMaGiC SN subsample, only one of 125 SNe has  $\log\text{Mass} < 10$ . In Figure 7, we show the logMass distributions for the full DES-5YR photometric sample and for the redMaGiC SN subsample (Smith et al. 2020b; Wiseman et al. 2020). About 90% of our redMaGiC sample have  $10.5 < \log\text{Mass} < 11.9$ , a much narrower range compared to the full DES-5YR photometric sample, which spans  $8 < \log\text{Mass} < 12$ . Due to the range of host galaxy masses for the redMaGiC subsample, it is impossible to measure the mass step, which is defined as the difference in intrinsic luminosity (after correction) between high-mass galaxies ( $\log\text{Mass} > 10$ ) and low-mass galaxies (Smith et al. 2020b). We expect that cosmological analyses using this subset of SNe Ia will be more robust to host galaxy stellar-mass dependencies, whereas here we use stellar mass as a proxy for other host galaxy properties. Future studies may also find it worthwhile to consider the homogeneity of other host galaxy properties, such as SFR or metallicity.

When  $\beta$  is floated in the BBC fit, we find  $\beta = 2.068 \pm 0.210$  for the redMaGiC sample, which is significantly smaller than  $\beta = 3.178 \pm 0.139$  for the DES-3YR spectroscopic sample (where  $\beta$  or  $R_B = R_V + 1$ ). Interestingly, Meldorf et al. (2022) find that the  $R_V$  distribution for redMaGiC galaxies is at the lower end of the  $R_V$  range for the DES host galaxy distribution ( $\overline{R_V} = 1.54 \pm 0.02$ ), whereas for the full distribution it is  $R_V = 2.61 \pm 0.07$ . This finding supports the prediction from Brout & Scolnic (2021) that the Hubble scatter versus color relation can be explained by differing dust properties from different host galaxy populations, as it shows a direct link between the low  $\beta$  found for a particular subset of galaxies and the low  $R_V$  predicted for this same set. Sullivan et al. (2010) found that SNe with low-sSFR host galaxies have lower  $\beta$  than SNe with high-sSFR hosts, and, consistently, Kelsey et al. (2021) found lower  $\beta$  in high-mass/redder rest-frame U–R galaxies than in low-mass/bluer U–R galaxies. This finding

indicates that our redMaGiC subsample of SNe is less sensitive to color.

### 5.1. Future Prospects

As described in Kessler et al. (2010), it is possible to use the SALT2 framework to fit a photometric redshift from the light curve simultaneously with  $x_1$ ,  $c$ ,  $m_B$ , and  $t_0$ . To improve the photo- $z$  precision and reduce the outliers, the host galaxy photo- $z$  can be used as a prior for this SN light-curve fit. This five-parameter fit is the technically correct method for accounting for redshift uncertainties, so that they can be propagated to other SALT2 fitted parameters and covariances. However, our attempts to implement these methods presented problems at high redshift, because only two passbands ( $i$  and  $z$ ) are within the SALT2 model range, which poorly constrains the SN color and redshift. In addition, the SALT2 model requires interpolations that result in occasional discontinuities in the model derivatives with respect to redshift, which can lead to pathological behavior in MINUIT. Further investigation into and resolution of these issues is beyond the scope of this paper, but should be considered for future work in photometric SN cosmology. An alternative method is to measure the redshift contribution to the distance modulus uncertainty empirically, as detailed in Section 4.2.1. A further area of follow-up that will be required is improved modeling and better understanding of the Hubble scatter discrepancy between the data and the simulations at high redshifts ( $z > 0.8$ ), as explained in Section 4.3.

SN Ia cosmology with the next-generation surveys in the era of LSST and Roman will require methods, such as the one presented here, that make full use of the photometric data, without the constraints imposed by the limits of spectroscopy. To make a simple forecast for LSST, we follow the simulations from the TiDES Collaboration (Swann et al. 2019; C. Frohmaier et al. 2022, in preparation)<sup>61</sup> using the Baseline 1.7 OpSim run. We assume that 6% of the LSST SNe Ia discovered are in LRGs and that the redMaGiC photo- $z$  resolution is  $\sigma_z = 0.02$ . In total, there are  $\sim 2.4$  million SNe Ia with two points of  $S/N > 5$  that pass the light-curve quality cuts, with 6% amounting to 144,000 SNe. Assuming a low- $z$  sample of 2400 SNe (1350 after cuts), to anchor the Hubble diagram (LSST–DESC Science Requirements Document; the LSST Dark Energy Science Collaboration et al. 2018), and a prior on  $\Omega_M$  of  $0.311 \pm 0.01$ , we recover an uncertainty on  $w$  of 0.017. This is  $\sim 1.5$  times smaller than the statistical constraint from the current sample of Pantheon+ SNe (Brout et al. 2022). For the same-size simulated sample using spectroscopic redshifts, we recover a comparable uncertainty on  $w$  of 0.018. Limiting the size of the sample to 72,000, 14,400, and 7200 (3%, 0.6%, and 0.3% of all LSST SNe, respectively), we recover uncertainties on  $w$  of 0.016, 0.019, and 0.021. This leveling out of the statistical uncertainty, despite the increase in sample size, likely shows the limiting impact of only 2400 low- $z$  SNe.

Mitra & Linder (2021) provide a quantitative requirement on the photo- $z$  systematics for LSST and Roman, and conclude that the redshift systematic from the LSST color-matched nearest neighbor photo- $z$  estimates must be reduced by an order of magnitude for unbiased SN Ia cosmology. However, they do

<sup>61</sup> [https://docushare.lsst.org/docushare/dsweb/Get/Document-37640/Frohmeier\\_TiDES.pdf](https://docushare.lsst.org/docushare/dsweb/Get/Document-37640/Frohmeier_TiDES.pdf)

not propagate photo- $z$  biases through the light-curve fits, resulting in more stringent redshift requirements, as they do not account for the redshift–color correction noted in Appendix A.1. Further studies and deeper understanding of the systematic uncertainties associated with photometric redshifts will be required to fully utilize the statistical power of such data sets. The appropriate treatment of photometric redshifts will require the inclusion of redshift in bias corrections (5D or 7D), rather than the 1D corrections used in this study. An alternative method is also presented in the zBEAMS hierarchical Bayesian formalism by Roberts et al. (2017). A Bayesian approach may improve the treatment of redshift errors and properly account for the redshift–color self-correction in data discussed in Appendix A.1.

With increasing numbers of SN observations, it will be possible to use a low-redshift sample that also contains only SNe Ia in LRGs, providing us with a full sample of SNe Ia exclusively in red galaxies. However, the impacts of systematic redshift errors are much stronger at low redshift (Wojtak et al. 2015; Davis et al. 2019), and the color–redshift relation that reduces the impact of biases in the DES redshift range may not be sufficient for the unbiased use of photometric redshifts at low  $z$ . Further studies will also be required to determine the effects of redshift biases on constraining a time-varying equation of state. Upcoming data releases from volume-limited low-redshift samples, such as the Zwicky Transient Factory (Dhawan et al. 2022) SN Ia sample, will include spectroscopic redshifts from the SN or host galaxy. Therefore, the most promising approach may be to combine a spectroscopic low- $z$  LRG SN sample with a photometric high- $z$  LRG SN sample. In the nearer future, with the year six analysis from DES and the redMaGiC run on the deep fields, the number of SNe Ia found to be hosted in red galaxies will increase. It may also be possible to investigate alternative methods of selecting LRGs in order to create a larger host galaxy sample. Another extension that will require further investigation would be whether other galaxy types besides LRGs can be similarly used to restrict the host galaxy type and reduce the photometric redshift bias. Last, it may be possible to include information about the distribution of the redshifts beyond individual redshifts, as is standard practice in other cosmology analyses, such as the  $3 \times 2$  pt probes. The application of information traditionally used for other cosmology probes—such as the redMaGiC catalogs—to SN Ia cosmology is a largely unexplored area with tremendous potential.

## 6. Conclusion

Using the DES-5YR photometric sample, we present a first proof of concept that SNe Ia in redMaGiC hosts are a promising new avenue for SN cosmology. We show that restricting SNe Ia to those with redMaGiC host galaxies serves as a useful cross-check for photometric classification, as they preferentially host only SNe Ia:  $\sim 3\%$  of redMaGiC SNe Ia are photometrically classified as non-Ia, compared to 8% of a simulated DES-5YR photometric SN sample with no classifier.

We further present our cosmological parameter results and biases from using redMaGiC host galaxy photo- $z$ . Using the redMaGiC photo- $z$  results in biases in  $w$  of  $\sim 0.01$  when run on the data, which is consistent with the expectations from the simulations. The Hubble scatter from data is 0.193 mag for the redMaGiC photo- $z$ , which is consistent with 0.201 mag obtained from the simulations. Our findings indicate that the

redMaGiC photo- $z$  can be used in a relatively unbiased manner with respect to spectroscopic redshifts. Last, we describe related extensions and potential future work using other sources of host galaxy redshift information. This work thus lays the essential groundwork for the future development of the use of photometric redshifts for SN Ia cosmology in time-domain surveys, particularly for LSST and surveys with Roman.

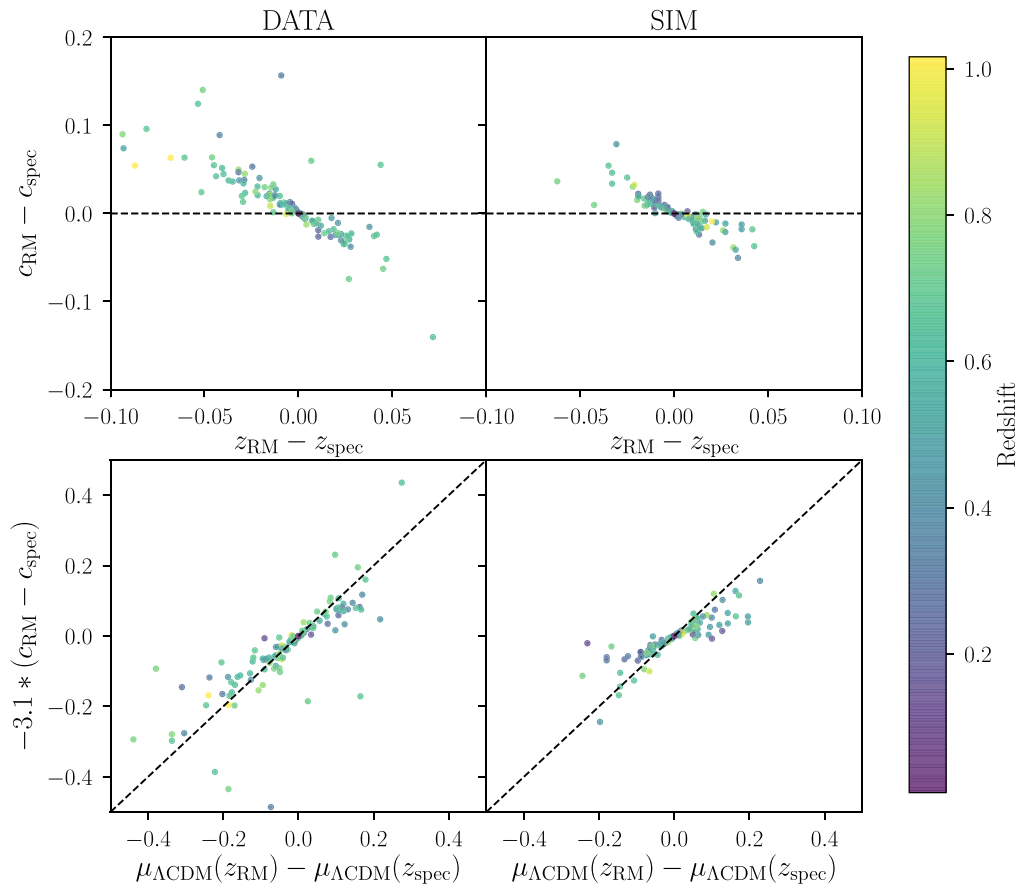
D.S. is supported by DOE grant No. DE-SC0010007 and the David and Lucile Packard Foundation. D.S. is supported in part by NASA under Contract No. NNG17PX03C, issued through the WFIRST Science Investigation Teams Programme. E. Rozo is supported by NSF grant No. 2009401. E. Rozo is further supported by DOE grant No. DE-SC0009913 and by a Cottrell Scholar award. L.K. thanks the UKRI Future Leaders Fellowship for support through grant No. MR/T01881X/1. L.G. acknowledges financial support from the Spanish Ministry of Science and Innovation (MCIN) under the 2019 Ramón y Cajal program RYC2019-027683-I and from the Spanish MCIN project HOSTFLOWS PID2020-115253GA-I00.

This paper has gone through internal review by the DES collaboration. Funding for the DES Projects has been provided by the U.S. Department of Energy, the U.S. National Science Foundation, the Ministry of Science and Education of Spain, the Science and Technology Facilities Council of the United Kingdom, the Higher Education Funding Council for England, the National Center for Supercomputing Applications at the University of Illinois at Urbana-Champaign, the Kavli Institute of Cosmological Physics at the University of Chicago, the Center for Cosmology and Astro-Particle Physics at the Ohio State University, the Mitchell Institute for Fundamental Physics and Astronomy at Texas A&M University, Financiadora de Estudos e Projetos, Fundação Carlos Chagas Filho de Amparo à Pesquisa do Estado do Rio de Janeiro, Conselho Nacional de Desenvolvimento Científico e Tecnológico and the Ministério da Ciência, Tecnologia e Inovação, the Deutsche Forschungsgemeinschaft, and the Collaborating Institutions in the Dark Energy Survey.

The Collaborating Institutions are Argonne National Laboratory, the University of California at Santa Cruz, the University of Cambridge, Centro de Investigaciones Energéticas, Medioambientales y Tecnológicas-Madrid, the University of Chicago, the University of Edinburgh, the Eidgenössische Technische Hochschule (ETH) Zürich, Fermi National Accelerator Laboratory, the University of Illinois at Urbana-Champaign, the Institut de Ciències de l’Espai (IEEC/CSIC), the Institut de Física d’Altes Energies, Lawrence Berkeley National Laboratory, the Ludwig-Maximilians Universität München and the associated Excellence Cluster Universe, the University of Michigan, NFS’s NOIRLab, the University of Nottingham, the Ohio State University, the University of Pennsylvania, the University of Portsmouth, SLAC National Accelerator Laboratory, Stanford University, the University of Sussex, Texas A&M University, and the OzDES Membership Consortium.

Based in part on observations at Cerro Tololo Inter-American Observatory at NSF’s NOIRLab (NOIRLab Prop. ID 2012B-0001; PI: J. Frieman), which is managed by the Association of Universities for Research in Astronomy (AURA) under a cooperative agreement with the National Science Foundation.

Based in part on data acquired at the Anglo-Australian Telescope, under program A/2013B/012. We acknowledge the



**Figure 8.** Top: redshift and color bias dependence, with the dashed black line at the color bias of zero, where the subscript “RM” stands for the redMaGiC photometric redshift case. Bottom: the  $\Lambda\text{CDM}$   $\mu$  bias plotted against the Tripp estimator term for color, with the dashed black line at  $x = y$ . Both are shown for data (left) and simulations (right). The color of each point corresponds to the redshift of the SN, as given by the colorbar on the right.

traditional owners of the land on which the AAT stands, the Gamilaraay people, and pay our respects to elders past and present.

The DES data management system is supported by the National Science Foundation under grant Nos. AST-1138766 and AST-1536171. The DES participants from Spanish institutions are partially supported by MICINN under grant Nos. ESP2017-89838, PGC2018-094773, PGC2018-102021, SEV-2016-0588, SEV-2016-0597, and MDM-2015-0509, some of which include ERDF funds from the European Union. IFAE is partially funded by the CERCA program of the Generalitat de Catalunya. Research leading to these results has received funding from the European Research Council under the European Union’s Seventh Framework Program (FP7/2007–2013), including ERC grant agreements 240672, 291329, and 306478. We acknowledge support from the Brazilian Instituto Nacional de Ciencia e Tecnologia (INCT) do e-Universo (CNPq grant 465376/2014-2).

This work was completed in part with resources provided by the University of Chicago’s Research Computing Center.

## Appendix

### A.1. Redshift Uncertainties and Redshift Color Dependencies

The formalism for uncertainty in  $\mu$  is typically described as given in Kessler et al. (2009a). However, in using the host galaxy photo- $z$  for this study, when naively including a  $\sigma_z^2$  term

in Equation (3), we find that the predicted uncertainty is overestimated compared to the true measured rms for  $\mu$  residuals. We show the cause of this overestimated uncertainty in Figure 8. When using the photo- $z$ , the dominant effect on the recovered distance is due to a change in the recovered color (following Equation (1)). While  $m_B$  and  $x_1$  are uncorrelated with redshift bias, the top right panel of Figure 8 shows that, for the simulations, the color parameter and redshift bias are correlated. As shown in the bottom panels of Figure 8, we find that the change in distance modulus  $\mu$  calculated from the fiducial  $\Lambda\text{CDM}$  model is roughly equal to the difference in color  $c$  multiplied by  $\beta$ , denoted as  $\beta \times \delta c$ . The left two panels in Figure 8 are made using the DES-5YR data, while the right two panels are made using our simulations. In practice, we can see on the Hubble diagram that misestimated redshifts correspond to a one-to-one self-correction in  $\mu$  along the  $\Lambda\text{CDM}$  curve. This trend is also observed in the data, with a redshift bias corresponding to a corrective bias in  $\mu$ .

We find that including the  $\sigma_z^2$  term is in general incorrect, as  $\mu$  and  $z$  are strongly correlated via the SALT2 color term. This change has a negligible effect on previous analyses performed with spectroscopic redshifts, as the redshift uncertainty for spec- $z$  is very close to zero. When the photometric redshift is misestimated, the light-curve fit returns a shifted color to compensate, which reduces the resulting scatter in the Hubble diagram.

We note that for peculiar velocities ( $v_{\text{pec}}$ ), the measured distance and redshift are independent, and therefore including

the  $\sigma_{\text{vpec}}$  term, as has previously been done, is appropriate. While this correction empirically works for the DES redshift range, we also note that it does not necessarily apply to low- $z$  SNe, which deviate further from a one-to-one correction. We further note that the relation may not be strictly linear; as the magnitude of the  $z_{\text{redmagic}} - z_{\text{spec}}$  bias increases past 0.05 or more, the deviation from a strict one-to-one relation does as well.

## A.2. Parent Population Parameters

Here, we present the parent population parameters for both the redMaGiC SNe (Table 8) and the full DES-3YR spectroscopic sample (Table 9) as a function of mass, and parametrized as described in Popovic et al. (2021). A summary of the average population parameters (described by a mean, left-sided  $\sigma_-$ , and right-sided  $\sigma_+$ ) is given in Table 2.




























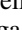


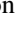

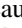






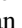




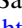
**Table 8**  
Parent Populations for the redMaGiC SN Sample

logMass	$c$			$x_1$		
	Mean	$\sigma_-$	$\sigma_+$	Mean	$\sigma_-$	$\sigma_+$
10.2	$-0.084 \pm 0.053$	$0.044 \pm 0.038$	$0.194 \pm 0.075$	$-1.798 \pm 0.769$	$1.69 \pm 0.821$	$2.002 \pm 0.618$
10.4	$-0.033 \pm 0.03$	$0.041 \pm 0.02$	$0.03 \pm 0.024$	$-0.254 \pm 0.615$	$1.72 \pm 0.652$	$0.627 \pm 0.486$
10.6	$-0.078 \pm 0.026$	$0.024 \pm 0.018$	$0.157 \pm 0.04$	$-0.528 \pm 0.712$	$1.467 \pm 0.619$	$0.808 \pm 0.543$
10.8	$-0.07 \pm 0.018$	$0.016 \pm 0.012$	$0.134 \pm 0.026$	$-0.464 \pm 0.68$	$1.512 \pm 0.57$	$0.762 \pm 0.534$
11.0	$-0.067 \pm 0.018$	$0.015 \pm 0.012$	$0.13 \pm 0.025$	$-0.453 \pm 0.685$	$1.462 \pm 0.55$	$0.747 \pm 0.543$
11.2	$-0.064 \pm 0.022$	$0.019 \pm 0.015$	$0.134 \pm 0.025$	$-0.66 \pm 0.741$	$2.093 \pm 0.617$	$1.272 \pm 0.556$
11.4	$-0.051 \pm 0.022$	$0.018 \pm 0.014$	$0.105 \pm 0.023$	$-1.338 \pm 0.851$	$1.81 \pm 0.769$	$1.742 \pm 0.66$
11.6	$-0.021 \pm 0.04$	$0.029 \pm 0.023$	$0.105 \pm 0.037$	$-1.34 \pm 0.766$	$1.574 \pm 0.826$	$2.11 \pm 0.6$
11.8	$0.09 \pm 0.098$	$0.139 \pm 0.071$	$0.19 \pm 0.076$	$-0.875 \pm 0.863$	$1.847 \pm 0.776$	$2.117 \pm 0.672$

**Table 9**  
Parent Populations for the DES-3YR Spectroscopic Sample

logMass	$c$			$x_1$		
	mean	$\sigma_-$	$\sigma_+$	mean	$\sigma_-$	$\sigma_+$
8.8	$-0.087 \pm 0.033$	$0.028 \pm 0.025$	$0.145 \pm 0.043$	$0.3 \pm 0.348$	$0.374 \pm 0.277$	$0.56 \pm 0.234$
9.0	$-0.091 \pm 0.025$	$0.021 \pm 0.018$	$0.139 \pm 0.035$	$0.28 \pm 0.312$	$0.331 \pm 0.23$	$0.535 \pm 0.216$
9.2	$-0.094 \pm 0.018$	$0.015 \pm 0.013$	$0.137 \pm 0.033$	$0.368 \pm 0.336$	$0.451 \pm 0.271$	$0.472 \pm 0.22$
9.4	$-0.1 \pm 0.02$	$0.017 \pm 0.014$	$0.169 \pm 0.035$	$0.233 \pm 0.338$	$0.387 \pm 0.255$	$0.677 \pm 0.234$
9.6	$-0.097 \pm 0.025$	$0.022 \pm 0.017$	$0.166 \pm 0.037$	$0.767 \pm 0.35$	$0.925 \pm 0.296$	$0.354 \pm 0.243$
9.8	$-0.089 \pm 0.022$	$0.02 \pm 0.015$	$0.158 \pm 0.033$	$0.712 \pm 0.369$	$1.146 \pm 0.321$	$0.378 \pm 0.258$
10.0	$-0.09 \pm 0.021$	$0.019 \pm 0.014$	$0.165 \pm 0.037$	$0.678 \pm 0.405$	$1.332 \pm 0.359$	$0.418 \pm 0.274$
10.2	$-0.099 \pm 0.021$	$0.019 \pm 0.014$	$0.204 \pm 0.037$	$0.502 \pm 0.51$	$1.323 \pm 0.442$	$0.536 \pm 0.331$
10.4	$-0.091 \pm 0.024$	$0.021 \pm 0.016$	$0.179 \pm 0.035$	$0.02 \pm 0.616$	$1.204 \pm 0.561$	$0.745 \pm 0.407$
10.6	$-0.075 \pm 0.028$	$0.026 \pm 0.019$	$0.147 \pm 0.033$	$-0.471 \pm 0.546$	$0.809 \pm 0.477$	$0.759 \pm 0.392$
10.8	$-0.087 \pm 0.016$	$0.012 \pm 0.01$	$0.128 \pm 0.04$	$-0.418 \pm 0.596$	$1.456 \pm 0.557$	$0.855 \pm 0.453$
11.0	$-0.077 \pm 0.021$	$0.018 \pm 0.014$	$0.133 \pm 0.041$	$-0.561 \pm 0.692$	$1.713 \pm 0.659$	$1.16 \pm 0.548$
11.2	$-0.062 \pm 0.034$	$0.031 \pm 0.025$	$0.153 \pm 0.049$	$-0.526 \pm 0.771$	$1.702 \pm 0.698$	$1.116 \pm 0.604$

## ORCID iDs

R. Chen  <https://orcid.org/0000-0003-3917-0966>  
 E. S. Rykoff  <https://orcid.org/0000-0001-9376-3135>  
 B. Popovic  <https://orcid.org/0000-0002-8012-6978>  
 R. Kessler  <https://orcid.org/0000-0003-3221-0419>  
 T. M. Davis  <https://orcid.org/0000-0002-4213-8783>  
 D. Brout  <https://orcid.org/0000-0001-5201-8374>  
 L. Galbany  <https://orcid.org/0000-0002-1296-6887>  
 C. Lidman  <https://orcid.org/0000-0003-1731-0497>  
 M. Sako  <https://orcid.org/0000-0003-2764-7093>  
 M. Sullivan  <https://orcid.org/0000-0001-9053-4820>  
 A. Carr  <https://orcid.org/0000-0003-4074-5659>  
 C. Conselice  <https://orcid.org/0000-0003-1949-7638>  
 K. Kuehn  <https://orcid.org/0000-0003-0120-0808>  
 G. F. Lewis  <https://orcid.org/0000-0003-3081-9319>  
 B. E. Tucker  <https://orcid.org/0000-0002-4283-5159>  
 M. Aguna  <https://orcid.org/0000-0001-5679-6747>  
 J. Annis  <https://orcid.org/0000-0002-0609-3987>  
 D. Bacon  <https://orcid.org/0000-0002-2562-8537>  
 E. Bertin  <https://orcid.org/0000-0002-3602-3664>  
 S. Bocquet  <https://orcid.org/0000-0002-4900-805X>  
 D. Brooks  <https://orcid.org/0000-0002-8458-5047>  
 J. Carretero  <https://orcid.org/0000-0002-3130-0204>  
 M. Costanzi  <https://orcid.org/0000-0001-8158-1449>  
 S. Desai  <https://orcid.org/0000-0002-0466-3288>  
 H. T. Diehl  <https://orcid.org/0000-0002-8357-7467>  
 J. García-Bellido  <https://orcid.org/0000-0002-9370-8360>  
 E. Gaztanaga  <https://orcid.org/0000-0001-9632-0815>  
 D. Gruen  <https://orcid.org/0000-0003-3270-7644>  
 S. R. Hinton  <https://orcid.org/0000-0003-2071-9349>  
 D. L. Hollowood  <https://orcid.org/0000-0002-9369-4157>  
 F. Menanteau  <https://orcid.org/0000-0002-1372-2534>  
 R. Miquel  <https://orcid.org/0000-0002-6610-4836>  
 R. Morgan  <https://orcid.org/0000-0002-7016-5471>  
 A. Palmese  <https://orcid.org/0000-0002-6011-0530>  
 F. Paz-Chinchón  <https://orcid.org/0000-0003-1339-2683>  
 A. Pieres  <https://orcid.org/0000-0001-9186-6042>  
 A. K. Romer  <https://orcid.org/0000-0002-9328-879X>  
 A. Roodman  <https://orcid.org/0000-0001-5326-3486>  
 S. Serrano  <https://orcid.org/0000-0002-0211-2861>  
 I. Sevilla-Noarbe  <https://orcid.org/0000-0002-1831-1953>  
 M. Smith  <https://orcid.org/0000-0002-3321-1432>  
 M. Soares-Santos  <https://orcid.org/0000-0001-6082-8529>  
 G. Tarle  <https://orcid.org/0000-0003-1704-0781>  
 D. Thomas  <https://orcid.org/0000-0002-6325-5671>  
 D. L. Tucker  <https://orcid.org/0000-0001-7211-5729>

## References

- Abbott, T., Alarcon, A., Allam, S., et al. 2019, *PhRvL*, 122, 171301  
 Abbott, T. M. C., Allam, S., Andersen, P., et al. 2019, *ApJL*, 872, L30  
 Astier, P., El Hage, P., Guy, J., et al. 2013, *A&A*, 557, A55  
 Astier, P., Guy, J., Regnault, N., et al. 2006, *A&A*, 447, 31  
 Betoule, M., Kessler, R., Guy, J., et al. 2014, *A&A*, 568, A22  
 Brout, D., Hinton, S. R., & Scolnic, D. 2021, *ApJL*, 912, L26  
 Brout, D., Sako, M., Scolnic, D., et al. 2019b, *ApJ*, 874, 106  
 Brout, D., & Scolnic, D. 2021, *ApJ*, 909, 26  
 Brout, D., Scolnic, D., Kessler, R., et al. 2019a, *ApJ*, 874, 150  
 Brout, D., Scolnic, D., Popovic, B., et al. 2022, arXiv:2202.04077  
 Cawthon, R., Elvin-Poole, J., Porredon, A., et al. 2022, *MNRAS*, 513, 5517  
 Chambers, K. C., Magnier, E. A., Metcalfe, N., et al. 2016, arXiv:1612.05560  
 Childress, M. J., Lidman, C., Davis, T. M., et al. 2017, *MNRAS*, 472, 273  
 Childress, M. J., Wolf, C., & Zahid, H. J. 2014, *MNRAS*, 445, 1898  
 Davis, T. M., Hinton, S. R., Howlett, C., & Calcino, J. 2019, *MNRAS*, 490, 2948  
 Dhawan, S., Goobar, A., Smith, M., et al. 2022, *MNRAS*, 510, 2228  
 Dore, O., Hirata, C., Wang, Y., et al. 2019, *BAAS*, 51, 341  
 Flaughner, B., Diehl, H. T., Honscheid, K., et al. 2015, *AJ*, 150, 150  
 Foley, R. J., & Mandel, K. 2013, *ApJ*, 778, 167  
 Foley, R. J., Scolnic, D., Rest, A., et al. 2018, *MNRAS*, 475, 193  
 Goldstein, D. A., D'Andrea, C. B., Fischer, J. A., et al. 2015, *AJ*, 150, 82  
 Gupta, R. R., Kuhlmann, S., Kovacs, E., et al. 2016, *AJ*, 152, 154  
 Guy, J., Astier, P., Baumont, S., et al. 2007, *A&A*, 466, 11  
 Guy, J., Sullivan, M., Conley, A., et al. 2010, *A&A*, 523, A7  
 Hakobyan, A. A., Barkhudaryan, L. V., Karapetyan, A. G., et al. 2020, *MNRAS*, 499, 1424  
 Hamuy, M., Trager, S. C., Pinto, P. A., et al. 2000, *AJ*, 120, 1479  
 Hinton, S., & Brout, D. 2020, *JOSS*, 5, 2122  
 Hložek, R., Ponder, K. A., Malz, A. I., et al. 2020, arXiv:2012.12392  
 Holtzman, J. A., Marriner, J., Kessler, R., et al. 2008, *AJ*, 136, 2306  
 Hounsell, R., Scolnic, D., Foley, R. J., et al. 2018, *ApJ*, 867, 23  
 Irani, I., Prentice, S. J., Schulze, S., et al. 2022, *ApJ*, 927, 10  
 Ivezić, Ž., Kahn, S. M., Tyson, J. A., et al. 2019, *ApJ*, 873, 111  
 Jones, D. O., Riess, A. G., Scolnic, D. M., et al. 2018, *ApJ*, 867, 108  
 Jones, D. O., Scolnic, D. M., Riess, A. G., et al. 2017, *ApJ*, 843, 6  
 Kelly, P. L., Hicken, M., Burke, D. L., Mandel, K. S., & Kirshner, R. P. 2010, *ApJ*, 715, 743  
 Kelsey, L., Sullivan, M., Smith, M., et al. 2021, *MNRAS*, 501, 4861  
 Kessler, R., Becker, A. C., Cinabro, D., et al. 2009a, *ApJS*, 185, 32  
 Kessler, R., Bernstein, J. P., Cinabro, D., et al. 2009b, *PASP*, 121, 1028  
 Kessler, R., Cinabro, D., Bassett, B., et al. 2010, *ApJ*, 717, 40  
 Kessler, R., Guy, J., Marriner, J., et al. 2013, *ApJ*, 764, 48  
 Kessler, R., Marriner, J., Childress, M., et al. 2015, *AJ*, 150, 172  
 Kessler, R., Narayan, G., Avelino, A., et al. 2019, *PASP*, 131, 094501  
 Kessler, R., & Scolnic, D. 2017, *ApJ*, 836, 56  
 Leaman, J., Li, W., Chornock, R., & Filippenko, A. V. 2011, *MNRAS*, 412, 1419  
 Lidman, C., Tucker, B. E., Davis, T. M., et al. 2020, *MNRAS*, 496, 19  
 Meldorf, C., Palmese, A., Brout, D., et al. 2022, arXiv:2206.06928  
 Mitra, A., & Linder, E. V. 2021, *PhRvD*, 103, 023524  
 Moller, A., & de Boissière, T. 2020, *MNRAS*, 491, 4277  
 Möller, A., Smith, M., Sako, M., et al. 2022, *MNRAS*, 514, 5159  
 Morganson, E., Gruendl, R. A., Menanteau, F., et al. 2018, *PASP*, 130, 074501  
 Nicolas, N., Rigault, M., Copin, Y., et al. 2021, *A&A*, 649, A74  
 Popovic, B., Brout, D., Kessler, R., Scolnic, D., & Lu, L. 2021, *ApJ*, 913, 49  
 Popovic, B., Scolnic, D., & Kessler, R. 2020, *ApJ*, 890, 172  
 Rigault, M., Aldering, G., Kowalski, M., et al. 2015, *ApJ*, 802, 20  
 Rigault, M., Brinnel, V., Aldering, G., et al. 2020, *A&A*, 644, A176  
 Rigault, M., Copin, Y., Aldering, G., et al. 2013, *A&A*, 560, A66  
 Roberts, E., Lochner, M., Fonseca, J., et al. 2017, *JCAP*, 2017, 036  
 Roman, M., Hardin, D., Betoule, M., et al. 2018, *A&A*, 615, A68  
 Roza, E., Rykoff, E. S., Abate, A., et al. 2016, *MNRAS*, 461, 1431  
 Rykoff, E. S., Roza, E., Busha, M. T., et al. 2014, *ApJ*, 785, 104  
 Rykoff, E. S., Roza, E., Hollowood, D., et al. 2016, *ApJS*, 224, 1  
 Sako, M., Bassett, B., Connolly, B., et al. 2011, *ApJ*, 738, 162  
 Scolnic, D., & Kessler, R. 2016, *ApJL*, 822, L35  
 Scolnic, D. M., Jones, D. O., Rest, A., et al. 2018, *ApJ*, 859, 101  
 Smith, M., D'Andrea, C. B., Sullivan, M., et al. 2020a, *AJ*, 160, 267  
 Smith, M., Sullivan, M., Wiseman, P., et al. 2020b, *MNRAS*, 494, 4426  
 Stoughton, C., Lupton, R. H., Bernardi, M., et al. 2002, *AJ*, 123, 485  
 Sullivan, M., Conley, A., Howell, D. A., et al. 2010, *MNRAS*, 406, 782  
 Sullivan, M., Le Borgne, D., Pritchet, C. J., et al. 2006, *ApJ*, 648, 868  
 Swann, E., Sullivan, M., Carrick, J., et al. 2019, *Msng*, 175, 58  
 The LSST Dark Energy Science Collaboration, Mandelbaum, R., Eifler, T., et al. 2018, arXiv:1809.01669  
 The PLAsTiCC team, Allam, T. J., Bahmanyar, A., et al. 2018, arXiv:1810.00001  
 Tripp, R. 1998, *A&A*, 331, 815  
 Vincenzi, M., Sullivan, M., Firth, R. E., et al. 2019, *MNRAS*, 489, 5802  
 Vincenzi, M., Sullivan, M., Graur, O., et al. 2021, *MNRAS*, 505, 2819  
 Vincenzi, M., Sullivan, M., Möller, A., et al. 2022, *MNRAS*  
 Wiseman, P., Smith, M., Childress, M., et al. 2020, *MNRAS*, 495, 4040  
 Wojtak, R., Davis, T. M., & Wiis, J. 2015, *JCAP*, 2015, 025  
 Yuan, F., Lidman, C., Davis, T. M., et al. 2015, *MNRAS*, 452, 3047